J. Fluid Mech. (2010), *vol.* 654, *pp.* 65–97.
doi:10.1017/S002211201000042X

Nonlinear dynamics and synthetic-jet-based control of a canonical separated flow

RUPESH B. KOTAPATI[1]†, RAJAT MITTAL[1]‡, OLAF MARXEN[2], FRANK HAM[2], DONGHYUN YOU[3] AND LOUIS N. CATTAFESTA III[4]

[1]Department of Mechanical and Aerospace Engineering, The George Washington University, Washington, DC 20052, USA

[2]Centre for Turbulence Research, Stanford University, Stanford, CA 94305, USA

[3]Department of Mechanical Engineering, Carnegie Mellon University, Pittsburgh, PA 15213, USA

[4]Department of Mechanical and Aerospace Engineering, University of Florida, Gainesville, FL 32611, USA

(Received 13 January 2009; revised 22 January 2010; accepted 23 January 2010; first published online 11 May 2010)

A novel flow configuration devised for investigation of active control of separated airfoil flows using synthetic jets is presented. The configuration consists of a flat plate, with an elliptic leading edge and a blunt trailing edge, at zero incidence in a free stream. Flow separation is induced on the upper surface of the airfoil at the aft-chord location by applying suction and blowing on the top boundary of the computational domain. Typical separated airfoil flows are generally characterized by at least three distinct frequency scales corresponding to the shear layer instability, the unsteadiness of the separated region and the vortex shedding in the wake, and all these features are present in the current flow. Two-dimensional Navier–Stokes simulations of this flow at a chord Reynolds number of 6×10^4 have been carried out to examine the nonlinear dynamics in this flow and its implications for synthetic-jet-based separation control. The results show that there is a strong nonlinear coupling between the various features of the flow, and that the uncontrolled as well as the forced flow is characterized by a variety of 'lock-on' states that result from this nonlinear coupling. The most effective separation control is found to occur at the highest forcing frequency for which both the shear layer and the separated region lock on to the forcing frequency. The effects of the Reynolds number on the scaling of the characteristic frequencies of the separated flow and its subsequent control are studied by repeating some of the simulations at a higher Reynolds number of 1×10^5.

1. Introduction

Prevention, delay or mitigation of flow separation over aircraft wings is an area of significant interest in aeronautics. Control of boundary-layer separation is effected by both passive and active mechanisms. Whereas passive techniques do not require additional power but have an associated drag penalty, active mechanisms require expenditure of energy, though much less than the energy gained by the effective control

† Present address: Exa Corporation, 55 Network Drive, Burlington, MA 01803, USA.
‡ Present address: Department of Mechanical Engineering, Johns Hopkins University, Baltimore, MD 21218, USA. Email address for correspondence: mittal@jhu.edu

of separation. Some of the most widely researched active separation control (ASC) techniques include moving walls (Prandtl 1925; Johnson, Tennant & Stamps 1975), suction (Prandtl 1904, 1935), direct tangential injection or wall jets (Delery 1985; Katz, Horev & Wygnanski 1992; Zhou & Wygnanski 1993), internal and external acoustic excitation (Collins 1979; Sigurdson & Roshko 1985), periodic forcing via vibrating flap (Neuburger & Wygnanski 1987), oscillating fence (Shepshelovich *et al.* 1989) or wire (Bar-Sever 1989), oscillatory surface heating (Maestrello, Badavi & Noonan 1988), and more recently, oscillatory blowing using zero-net-mass-flux (ZNMF) or synthetic jets (Seifert *et al.* 1993; Seifert, Darabi & Wygnanski 1996; Amitay *et al.* 1997; Seifert, Eliahu & Greenblatt 1998; Seifert & Pack 1999; Chatlynne *et al.* 2001). Gad-El-Hak & Bushnell (1991) and Gad-El-Hak (2000) review the state of the art in separation control using both passive and active mechanisms.

Experiments by Neuburger & Wygnanski (1987), Shepshelovich *et al.* (1989), Bar-Sever (1989) and Seifert *et al.* (1993), using very different active mechanical devices embedded in the boundary layer, strongly demonstrated that separation can be delayed and sometimes completely prevented by introducing strong oscillations in the region of incipient separation. Studies by Nishri (1995) show that the nature of the device used to generate these oscillations is not important as long as the vorticity fluctuations introduced in the region of incipient separation are similar. Of the different techniques available for introducing such periodic perturbations into the boundary layer, synthetic jets (or more generally, ZNMF jets) have emerged as effective for separation control owing to the following factors: they allow independent control of the excitation magnitude and frequency; inclusion of ZNMF actuators for oscillatory blowing leaves the airfoil geometry almost unchanged with little weight penalty; the actuators are fairly robust and their performance does not attenuate with increased aerodynamic loading (Seifert *et al.* 1998). Research on these actuators has primarily been directed towards understanding the associated flow physics with the objective of identifying optimal forcing schemes and the following discussion summarizes our current understanding and some of the outstanding issues in this area.

1.1. *Flow physics of ZNMF-based separation control*

Experimental investigations (Seifert & Pack 1999; Glezer, Amitay & Honohan 2003) have shown that accelerated or forced laminar–turbulent transition does not play a pivotal role in synthetic-jet-based (SJ-based) separation control. A fundamental mechanism that is often identified in SJ-based separation control is the formation of large coherent structures in the separated shear layer due to oscillatory forcing. These structures entrain outer high-momentum fluid into the boundary layer, thereby delaying separation or even reattaching a separated flow. However, the effectiveness of this mechanism relies on the receptivity of the mean flow to the imposed oscillations which in turn depends on the stability characteristics of the separated flow. Thus, to be effective, the perturbations have to be of appropriate frequency and sufficient amplitude and be introduced at the right location in the boundary layer (Seifert *et al.* 1996). The successful control of boundary-layer separation using SJ actuators is determined by a multitude of parameters: the ratio of the SJ velocity to the free-stream velocity, V_J/U_∞ (or alternatively the oscillatory blowing momentum coefficient, $C_\mu = \rho V_J^2 d/(q_\infty c)$); the dimensionless frequency of the jet, F_J^+; relative location of the actuator on the surface, x_J; the shape (curvature), thickness ratio and incidence of the airfoil that determine the adversity of the pressure gradient; the Reynolds number and Mach number of the flow; and several other parameters thought to be

of second-order importance such as the inclination of the actuator slot to the wetted surface, etc.

For an SJ of a given width, the key operational parameters are the jet frequency f_J and the jet velocity V_J. The former is usually non-dimensionalized as $F_J^+ = f_J/f_n$, where f_n is a frequency associated with some intrinsic time scale in the uncontrolled flow. The parameter V_J is some characteristic measure of the jet velocity, such as the peak or an average velocity during the discharge phase of the cycle, and is normalized by U_∞. The control authority has been found to vary monotonically with V_J (Seifert *et al.* 1993, 1996; Seifert & Pack 1999; Glezer & Amitay 2002) up to a point where any further increase leads to a complete disruption of the boundary layer. Moreover, the hardware limitations of typical SJ devices do not allow realization of large jet velocities. Therefore, there is very little leeway for optimizing the SJ device with respect to V_J. On the other hand, control authority has been found to exhibit a highly non-monotonic variation with F_J^+ (Seifert & Pack 2000; Greenblatt & Wygnanski 2003; Glezer *et al.* 2003), and this not only suggests the presence of rich flow physics and a highly nonlinear multi-modal system, but also reveals the potential for optimizing the control scheme with respect to this parameter. The various issues pertinent to the flow physics of separation control are discussed below.

1.1.1. *Constituents of a separated airfoil flow*

Separation control schemes that harness large vortical structures to transfer momentum from the outer flow into the boundary layer are based on the proposition that the dynamics of a separated flow over an airfoil are dominated by the characteristic frequency of the separation region denoted here by f_{sep}. On the contrary, in addition to f_{sep}, there are other naturally occurring frequencies that can play an important role in the dynamics of the flow. To examine this further, it is useful to classify the types of separation encountered for typical airfoils, and the subsequent discussion is drawn from classical work on stall classification by McCullough & Gault (1951), Chang (1976), and more recent work on temporal dynamics of stalled airfoil flows by Zaman, McKenzie & Rumsey (1989), Broeren & Bragg (1998), Bragg, Hienrich & Khodadoust (1993), Bragg *et al.* (1996) and Wu *et al.* (1998). Based on these previous studies, one can consider the following three situations with regards to separation control as shown in figure 1. Case A represents attached flow over a thin airfoil at low angle-of-attack (AOA) where the boundary layer on the suction side develops under an adverse pressure gradient but does not separate. Such a flow has one dominant time scale characterized by the inverse of the wake vortex shedding frequency f_{wake}.

In direct contrast to Case A is the situation of a massively separated post-stall flow at high AOA, portrayed as Case C, where separation occurs near the leading edge and the flow does not reattach (in the mean) to the airfoil surface. This flow behaves like that past a bluff body and is consequently subject to two frequency scales, f_{SL} and f_{wake}, where the former is the natural vortex roll-up frequency of the shear layer and the latter is again the frequency corresponding to vortex shedding in the wake. A number of experimental investigations of bluff-body wakes (Kourta *et al.* 1987; Williamson, Wu & Sheridan 1995; Prasad & Williamson 1996; Wu *et al.* 1996) have shown that such a local convective instability mechanism of the shear layer is indeed important even in the presence of the global absolute instability of the wake. An extensive survey of the literature in this area reveals that only Wu *et al.* (1998) have considered both f_{SL} and f_{wake} in their studies. In contrast, other studies of post-stall separation control account for f_{wake} but do not consider f_{SL} (He, Cary & Peters

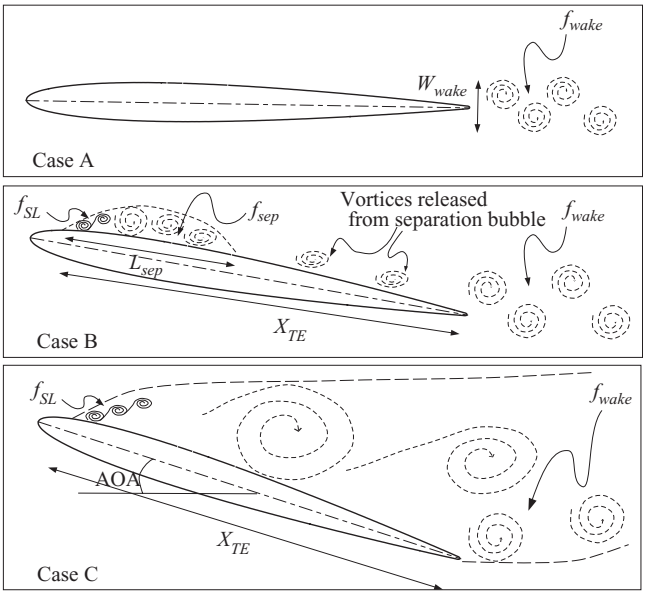

FIGURE 1. Schematic of the three different scenarios for flow past an airfoil.

2001; Miranda, Telionis & Zeiger 2001; Chen & Beeler 2002). Finally, a majority of studies that have examined massively separated flow past airfoils with deflected flaps (e.g. Seifert *et al.* 1993, 1996; Wygnanski 1997) consider only a single frequency corresponding to the separation region, f_{sep}, which is not necessarily the same as either f_{wake} or f_{SL}.

Finally, Case B corresponds to the situation where separation occurs at some location downstream of the leading edge, and the separated shear layer may or may not reattach before the trailing edge. For instance, on some thin airfoils (like the NACA 0012), stall is manifested through the appearance of a small separation bubble near the leading edge (Chang 1976). On the other hand, open separation zones near the trailing edge can be found on thicker airfoils (Chang 1976; Greenblatt & Wygnanski 2003) and on the exposed portion of low-pressure turbine (LPT) blades (Mittal, Venkatasubramanian & Najjar 2001; Postl, Gross & Fasel 2004). If the separated shear layer reattaches before the trailing edge, there are potentially three frequency scales: f_{wake}, f_{SL}, and f_{sep}, the frequency scale corresponding to the regular expulsion of large vortices from the separated region. The resonant interaction between these different processes is a strong function of the distance between the separation location and the trailing edge, x_{TE}. It also depends on whether the separation bubble extends to the trailing edge or closes far upstream of it. When the separated shear layer does not reattach and the separation is of the open type, the flow is similar to Case C except that the separation point is not fixed at the leading edge. Mittal *et al.* (2001) examined the scaling of the frequencies for a PAK-B, LPT blade via large-eddy simulations and found that the wake, indeed, plays a role in determining the dynamics of suction-side separation.

In summary, therefore, f_{sep} is only one of at least three potentially naturally occurring frequencies in a separated airfoil flow. Therefore, it is quite possible that these different processes modulate each other even as they evolve because of nonlinear coupling between them (Wu *et al.* 1998). However, the current understanding of the dynamics of these processes is quite limited.

1.1.2. *Scaling of characteristic frequencies*

Consider the flow over an airfoil at incidence where the separation occurs at some location downstream of the leading edge, and the separated shear layer may or may not reattach before the trailing edge. For a shear layer that separates from and reattaches to a solid surface (as in Case B in figue 1), the presence of a near-wall reversed flow region permits upstream propagation of disturbances and alters the stability characteristics of the shear layer. In this case, the frequency corresponding to the separated region scales as $f_{sep} \sim U_\infty / L_{sep}$, where L_{sep} is the characteristic length of the mean separation bubble. Numerical investigations of separated flow past a wall mounted tab (Auld & Mittal 1999) and flow past a normal flat plate with a wake splitter (Najjar & Vanka 1993) indicate a universal value of $f_{sep} L_{sep} / U_\infty \approx 0.27$ when L_{sep} is defined as the distance between the separation point and the centre of the mean recirculation bubble. It is plausible that in such cases f_{SL} locks-on to f_{sep} through subharmonic resonance (Ho & Huang 1982).

For a shear layer that separates and does not reattach (as in Case C in figure 1), the shear layer instability plays an important role. The corresponding frequency scales more like that of a free shear layer (Ho & Huerre 1984), i.e. $f_{SL} \sim \bar{U}/\theta$, where $\bar{U}$ is the average velocity across the shear layer and θ is the momentum thickness. In fact, Ho & Huerre (1984) have shown that $f_{SL}\theta/\bar{U}$ attains a nearly universal value of about 0.03 for a laminar flow and about 0.04 for a turbulent flow. In the special case where such shear layers are part of a Kármán-type vortex shedding process, as would be the situation in Case C, the above scaling can be reformulated as $f_{SL} = ARe^B f_{wake}$ (Kourta *et al.* 1987; Williamson, Wu & Sheridan 1995; Wu, Sheridan, Hourigan & Soria 1996) where the Reynolds number accounts for the dependence of the frequency on the momentum thickness. For a circular cylinder, $A \approx 0.024$ and $B \approx 0.67$ (Prasad & Williamson 1996).

The wake vortex shedding resulting from absolute instability, however, is active for all cases and due to its global effect, probably plays some role in the dynamics of the flow. The scaling for Kármán vortex shedding due to Roshko (1954) is $f_{wake} \sim U_\infty / W_{wake}$, where W_{wake} is the characteristic width of the wake, and this scaling is fundamentally different from that of f_{sep}. In many studies (Wu *et al.* 1998; Miranda *et al.* 2001), W_{wake} is assumed to be equal to $c\sin(\alpha)$ where c is the airfoil chord length and α is the angle of attack. In cases where the separation extends over a significant portion of the airfoil (or a flap), it has been customary to assume $L_{sep} = c$ (Bar-Sever 1989; Seifert *et al.* 1993; Ravindran 1999; Wygnanski 2000; Darabi & Wygnanski 2002; Funk *et al.* 2002; Postl *et al.* 2004), but this might significantly overestimate the correct length scale in cases where the wake vortex shedding dominates the dynamics.

1.1.3. *Effective forcing frequency*

Given the multi-frequency nature of the separated flow system and the different scalings of the characteristic system frequencies depending on the type of separation, the situation with regard to the optimal forcing frequency is not quite obvious. Experiments by Seifert *et al.* (1993, 1996) suggest that the frequency that will elicit the largest response is the one for which the streamwise length of separated flow requiring control (i.e. L_{sep}) is comparable to the average wavelength of the imposed oscillations. This implies that $F_J^+ = f/f_{sep} = fL_{sep}/U_\infty \sim O(1)$. However, even if one were to account for the various length scales used in the definition of F_J^+, there is still a wide variation in the observed values of optimal F_J^+. For example, among studies that have defined $F_J^+ = fc/U_\infty$, where c is airfoil or flap chord over which flow is fully separated, optimal F_J^+ values ranging from 0.55 to 5.5 have been observed

(Bar-Sever 1989; Seifert *et al.* 1993; Ravindran 1999; Wygnanski 2000; Darabi & Wygnanski 2002; Funk *et al.* 2002; Margalit *et al.* 2002). Among studies that define $F_J^+ = f x_{TE}/U_\infty$, where x_{TE} is streamwise distance between the actuator and the trailing edge, optimal values of F_J^+ range from 0.5 to 2.0 (Greenblatt & Wygnanski 1999; Seifert & Pack 1999; Gilarranz & Rediniotis 2001). Finally, for studies that employ $F_J^+ = f L_{sep}/U_\infty$, optimal values ranging from 0.75 to 2.0 have been reported (Seifert *et al.* 1996; Pack & Seifert 2000; Pack *et al.* 2002). It may seem that the magnitude of the variation in optimal value of F_J^+ reported in these studies is not significant, except that in many cases the control authority of the SJ device varied considerably with small changes in F_J^+. For instance, Seifert *et al.* (1993) reported a 25 % variation in C_L as F_J^+ varied between 0.25 and 1.5, while Wygnanski (2000) found that the required C_μ increased by about 400 % for the same variation in F_J^+.

For post-stall applications similar to Case C, Wu *et al.* (1998) have argued that the most effective control frequency should be a superharmonic of f_{wake}, i.e. $F_J^+ = f/f_{wake} = m$, where m is an integer greater than 1. Due to the ability of the shear layer to respond to a broad range of frequencies, it is expected that a suitable choice of m can allow both the vortex shedding and shear layer to lock on to the forcing frequency or its superharmonic. Lack of consideration of the importance of f_{wake} and the associated resonant interactions with f_{sep} in past studies (Seifert *et al.* 1993, 1996; Wygnanski 1997; Seifert & Pack 1999) might explain some of the spread in optimal F_J^+ and corresponding C_μ values reported in the literature.

Wide disparities in the past investigations of active ASC with respect to the above considerations motivate systematic studies in simple configurations that eliminate confounding variables and clearly delineate various physical mechanisms that are potentially implicated in ASC. The primary objective of this work is to employ a novel flow configuration that allows us to (i) examine the dynamics of baseline aft-chord separated flow to determine the nature of the nonlinear coupling between the various instabilities that exist in the flow, (ii) investigate the effects of forcing frequency F_J^+ in light of these nonlinear coupling mechanisms.

2. Flow configuration

The previous section described some of the key outstanding technical issues in the area of ASC using SJ actuators. Past approaches to studying these issues have mostly employed conventional airfoil geometries where the flow separation is produced by varying AOA and/or free-stream velocity. Although this approach is grounded in practical reality, it does not facilitate precise investigation and delineation of the various physical mechanisms that are potentially implicated in ASC. As discussed in the preceding section, the separated flow over an airfoil is a complex system with potentially three different naturally occurring frequencies. In order to examine the scaling of these frequencies as well as their potential nonlinear interactions, it would be extremely useful to separately prescribe the extent and location of the separation bubble as well as the Reynolds number. This is not possible through simple variation of AOA and/or free-stream velocity for an airfoil. Therefore, a flow configuration is needed that is simple and includes all the important features of a separated airfoil flow such as the leading-edge boundary-layer inception, open or closed suction side separation and a wake that includes vortices from both the suction and pressure sides. Furthermore, such a configuration should also allow independent prescription of the location and extent of the separation region as well as the Reynolds number. It should be pointed out that some past studies have induced separation on a flat wall

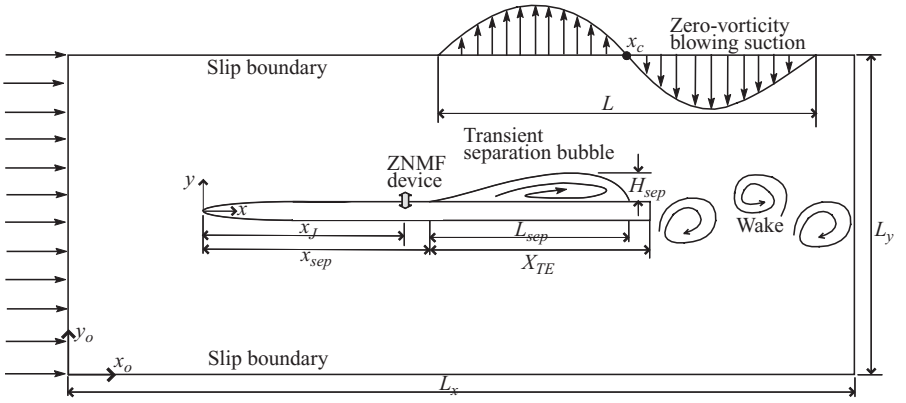

FIGURE 2. Schematic of the flow configuration (not to scale).

via modification of the upper boundary (Na & Moin 1998; Sohn, Shyne & DeWitt 1998; Postl *et al.* 2004) to impose adverse pressure gradient. This approach however does allow for independent control over the location and extent of the separation bubble but does not account for leading- and trailing-edge effects, pressure side boundary layer and its interaction with a two-sided wake.

Here, a novel configuration that satisfies all of the above requirements and is amenable to both computational fluid dynamics and experimentation is proposed. The focus of the current work is on numerical simulations and figure 2 shows a schematic of this flow configuration used in the simulations. It consists of a 5 % thick spanwise homogeneous flat-plate airfoil of chord c with 8:1 elliptic leading edge and blunt trailing edge at 0° AOA in a free stream. The blunt trailing edge is chosen to fix the separation point of the lower- and upper-side shear layers at the sharp corners of the trailing face, and provide unambiguous definition for the characteristic width of the wake. The origin of the global coordinate system (x_0, y_0, z_0) is fixed at the lower left-hand corner in the mid-span of the computational domain that measures L_x, L_y and L_z in X, Y and Z directions, respectively. The origin of the local coordinate system (x, y, z) is at the leading edge of the airfoil in the same mid-span plane. Note that x, y and z are in the streamwise, cross-stream and spanwise directions, respectively.

A separation bubble of desired size can be induced at any location on the upper surface of the flat plate by applying an adverse pressure gradient through suction and blowing on the upper boundary of the computational domain. The technique of Na & Moin (1998) is adopted wherein a zero-vorticity boundary condition of the following form is prescribed on the upper boundary:

$$v(x_0, L_y) = G(x_0), \qquad \left.\frac{\partial u}{\partial y_0}\right|_{(x_0, L_y)} = \frac{\mathrm{d}G}{\mathrm{d}x_0}, \tag{2.1}$$

where $G(x_0)$ is the prescribed steady suction and blowing velocity profile, and the Neumann boundary condition on u ensures that no spanwise vorticity (ω_z) is generated due to suction and blowing. In this study, $G(x_0)$ is of the form

$$G(x_0) = -V_{top} \sin\left(\frac{2\pi(x_0 - x_c)}{L}\right) \mathrm{e}^{-\alpha((2(x_0 - x_c))/L)^{\beta}}, \tag{2.2}$$

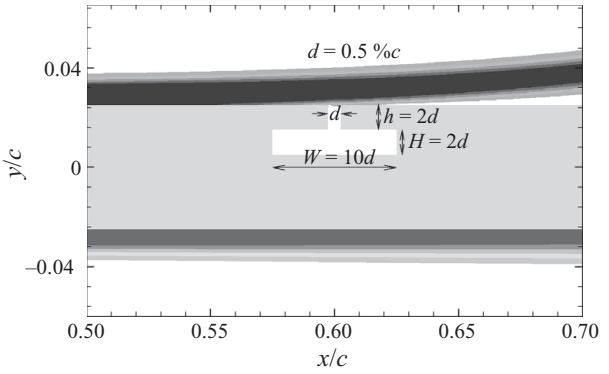

FIGURE 3. Schematic of the ZNMF actuator embedded in the airfoil.

where x_c is the centre of the steady suction and blowing velocity profile in the global system and L is the length of the profile (see figure 2). The function $G(x_0)$ allows independent prescription of the location as well as the streamwise size of the separation region by varying x_c and L. In (2.2), the sinusoidal function that models the suction and blowing profile is multiplied by an exponential blending function to provide continuity at the edges of the profile as it transitions to slip boundary condition on either side. The parameters V_{top}, α and β are set to $0.8U_\infty$, 10 and 20, respectively. Thus, separation can be produced anywhere on the plate surface and can therefore reproduce any of the three separated flow situations discussed in § 1.1.1. The above configuration can be used to examine the nonlinear interactions between the shear layer, separation region and airfoil wake in controlled as well as uncontrolled versions of these flows. It should be noted that with this configuration, the confounding effect of curvature is eliminated, something that is usually not possible with conventional airfoil geometries.

Rather than simply model the SJ by prescribing a localized analytical velocity profile (Rizzetta & Visbal 2004) on the flat plate, the flow inside the SJ actuator and the resulting SJ are simulated in the current study. This is done by embedding a slot and cavity under the upper surface of the flat plate as shown in figure 3. The ZNMF 'device' consists of a rectangular slot, of width $d = 0.005c$ and height $h = 2d$, connected to an internal rectangular cavity of width $W = 10d$ and height $H = 2d$. The choice of these dimensions for the SJ 'device' is driven by the design of an actuator used by Schaeffler, Jenkins & Hepner (2004) in the NASA LaRC 2004 workshop on computational fluid dynamics validation of SJs and turbulent separation control. In the experiments, the SJ through the slot is usually generated by the motion of a piston or a piezoelectric diaphragm mounted to the sides or the bottom of the cavity. In the computations, a simple oscillatory velocity boundary condition of the form $[u, v] = [0, V_0 \sin(2\pi f_J t)]$ is prescribed at the lower horizontal boundary of the cavity, where V_0 is the velocity amplitude and f_J is the oscillation frequency. This boundary condition essentially provides a simple sinusoidal representation of the mass flux produced in the slot by the motion of the piston or diaphragm in the experiments.

The characteristic velocity of the SJ is given by

$$V_J = \frac{2}{AT} \int_0^{T/2} \int_A v^e(x, t)\, \mathrm{d}A\, \mathrm{d}t, \tag{2.3}$$

where $v^e(x,t)$ is the y component of the velocity at the exit plane of the orifice, A is the cross-sectional area of the orifice and $T = 1/f_J$ is the time period of the SJ cycle. In the current incompressible simulations, the velocity amplitude at the lower boundary of the cavity V_0 is related to the characteristic jet velocity V_J through mass conservation by $V_0 = (\pi V_J/2)(d/W)$. Thus, V_J can be prescribed by applying a suitable value of V_0.

Uniform inflow free-stream velocity is prescribed at the inlet of the computational domain. At the exit boundary, a convective outflow boundary condition (Kaltenbach *et al.* 1999) is applied, with the convection speed determined by the streamwise velocity averaged across the exit plane. This outflow boundary condition allows the vortical structures from the separated region and the wake to exit the domain with minimal reflections. No-slip boundary condition is applied on the airfoil surface, and slot and cavity walls. Slip (zero-shear) boundary condition is applied over the entire length of the lower boundary.

3. Computational method

3.1. *Numerical algorithm*

The two-dimensional flow field in the above flow configuration is obtained by solving the governing unsteady incompressible Navier–Stokes equations, written in dimensional tensor form as

$$\frac{\partial u_i}{\partial x_i} = 0, \tag{3.1}$$

$$\frac{\partial u_i}{\partial t} + \frac{\partial u_i u_j}{\partial x_j} = -\frac{1}{\rho}\frac{\partial p}{\partial x_i} + \nu \frac{\partial^2 u_i}{\partial x_j \partial x_j}, \tag{3.2}$$

where x_i are the Cartesian coordinates, t is the time, p is the pressure and u_i are the Cartesian velocity components.

The flow field is computed using CDP (CDP is named after Charles David Pierce (1969–2002)), a hybrid unstructured grid finite-volume-based flow solver being actively developed at Stanford University's Centre for Integrated Turbulence Simulations (CITS) as part of the US Department of Energy's (DOE's) Advanced Simulation and Computing (ASC) programme. Details of the finite volume operators and boundary condition implementation are available elsewhere (Ham, Mattson & Iaccarino 2006). A key feature of this solver is that it uses central differences for spatial discretization and constrains the numerical scheme to discretely conserve not only mass and momentum, but also kinetic energy (Ham & Iaccarino 2004). This approach minimizes nonlinear instabilities that might arise from the complete absence of numerical dissipation at coarse-grid resolutions. For parallel implementation, the parallel graph partitioning library ParMETIS (Karypis, Schlogel & Kumar 2003) is used for domain decomposition and provides optimal load balancing with a minimal surface interface between zones. Communication between processors is achieved using Message Passing Interface (MPI) programming model.

3.2. *Simulation overview*

The current configuration has a number of flow parameters which can be varied to produce a wide variety of separated flow configurations. These parameters include the chord Reynolds number, and the location and extent of the blowing suction profile on the top boundary of computational domain which control the location and size of the separation bubble. The first objective of the current paper is to examine the rich

nonlinear dynamics of this flow which we have argued is generally representative of separated airfoil flows. The second objective is to conduct numerical flow control experiments and interpret the results in light of the observed nonlinear dynamics of the flow. As such, we have limited the current paper to one case where the separation bubble is created on the aft one-third of the flat plate. From a practical point of view, this case is representative of the aft-chord separation that is found on LPT blades. From a fundamental flow-physics viewpoint, the proximity of the separation bubble to the wake for this case should produce rich nonlinear interactions in the flow.

Apart from affecting the relative importance of inertial and viscous forces, the Reynolds number has a much more direct impact on the nonlinear dynamics of the flow. This is because, the three frequency scales in the flow have different dependencies on the Reynolds number. Whereas the wake and separation zone time scales are mostly independent of the Reynolds number, the frequency of the shear layer has a strong dependence on the Reynolds number. Thus, a variation in the Reynolds numbers (while keeping all other parameters fixed) can potentially alter the nonlinear interaction between the different features in the flow. In the current study, we primarily focus on a case with $Re = 6 \times 10^4$. This Reynolds numbers is high enough that it provides adequate separation between the time scales of the shear layer and the separation bubble, and at the same time, it is low enough to allow for an accurate high-fidelity Navier–Stokes computations. We also present results at $Re = 1 \times 10^5$ in order to examine the effect of this parameter.

All of the simulations presented in the current paper are two-dimensional and do not allow for spanwise variations in the flow. This allows us to focus on the vortex dynamics of the large-scale vortex structures without the complicating influence of transition and turbulence. Limited three-dimensional large-eddy simulations of the same flow have been performed (Kotapati 2008; Kotapati, Mittal & Ham 2008) and they indicate that the essential features of the nonlinear dynamics are not significantly affected.

The flat-plate airfoil geometry is centred in a computational domain of size $L_x \times L_y = 2c \times 0.5c$, and the aft-chord separation is induced by prescribing simultaneous blowing and suction over $0.7 \leqslant x/c \leqslant 1.3$ on the top boundary of the computational domain. In all of the simulations of the baseline separated flow presented here, the non-operational SJ 'device' embedded under the airfoil upper surface is left open to the external crossflow. Comparison of the location of boundary-layer separation obtained from such a simulation with one obtained without an embedded SJ cavity indicates that the inclusion of an inactive SJ device open to the external crossflow in the uncontrolled simulation does not change the separation location.

Firstly, the uncontrolled version of the flow configuration with aft-chord separation (hereafter referred to as 'Case 0') is computed at $Re = 6 \times 10^4$ to determine the characteristic frequency scales in the baseline separated flow. The simulations are performed on two different unstructured grids to ascertain the grid independency of the simulation results with respect to the characteristic frequency scales, separation and reattachment points, pressure and skin-friction distributions, etc. The unstructured grids are composed of hexahedral volumes and the details of grid spacing and resolution in key areas for these two grids are summarized in table 1. Several coarser grid simulations were carried out to determine the resolution requirements in critical flow regions such as the separated region, wake, etc, and this information was used in arriving at the baseline resolution of Grid I. Based on the local gradients in the boundary layer and the resolution characteristics of the flow solver, it was determined that the wall-parallel spacing on the flat surface of Grid I was over-resolved while

Attribute	Grid I	Grid II	Grid III
Overall node count	445 746	540 650	844 180
Nodes in wake region	66 306	99 330	99 330
Nodes in separated region	70 418	76 586	157 290
Nodes in SJ slot	1554	1554	1554
Nodes in SJ cavity	11 174	8806	8806
Wall parallel spacing on flat plate, $\Delta x/c$	0.0001–0.006	0.00025–0.0065	0.0001–0.006
Wall normal spacing on flat plate, $\Delta y/c$	2.5×10^{-4}	2.5×10^{-4}	1.25×10^{-4}

TABLE 1. Details of grids used in two-dimensional Navier–Stokes simulations.

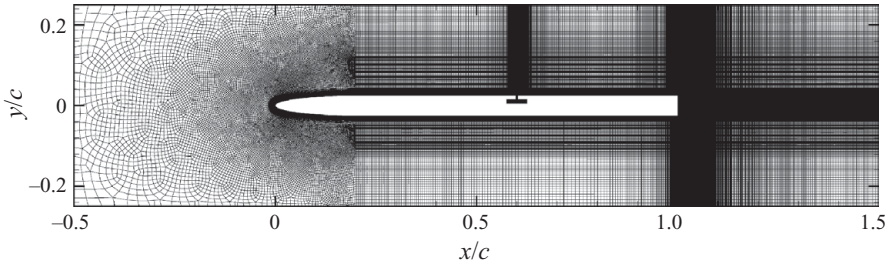

FIGURE 4. Computational mesh in the x–y plane of Grid II used in LES at $Re = 6 \times 10^4$.

the x-spacing in near-wake was only marginal. Therefore, Grid I was subsequently refined in the near-wake region by 50 % in both x and y directions, and relaxed in the over-resolved regions to yield nominal Grid II. Thus, even though the total number of grid points for Grids I and II are different by about 20 %, the distribution of the grid points in the critical regions such as in the wake is significantly different between the two grids. Figure 4 shows the computational mesh in the x–y plane of Grid II used in the simulations at $Re = 6 \times 10^4$.

The simulations are advanced with a time step of $\Delta t U_\infty/c = 2.0 \times 10^{-4}$, which corresponds to a maximum Courant–Friedrichs–Lewy (CFL) number of less than 2.8 and 1.7 on Grids I and Grid II, respectively. The simulations are typically carried out for at least a time period of $20c/U_\infty$, of which the last 10 time units are used for the computation of flow statistics discussed in § 4.1. Each simulation on Grid II requires over 500 single-node CPU hours, whereas a single simulation on Grid III takes over 800 single-node CPU hours.

The characteristic frequencies of the baseline separated flow are determined by computing one-dimensional power spectra E_{vv} corresponding to temporal variations of cross-stream velocity v in the shear layer, the separated region, and the wake. Flow state from Case 0 simulation at $t = 20c/U_\infty$ is then advanced with SJ perturbation of the boundary layer at frequencies that are harmonically related to the characteristic frequencies of the baseline separated system. The specific details of the forcing frequencies and their relation to baseline characteristic frequencies are discussed in the next section. In the simulations with SJ forcing, the time step employed is the same as in the baseline simulations and the SJ velocity is set to $V_J = 0.1U_\infty$. The blowing momentum coefficient of the jet is defined as

$$c_\mu = \frac{\rho V_j^2 d}{qc} = 2\frac{d}{c}\left(\frac{V_J}{U_\infty}\right)^2, \tag{3.3}$$

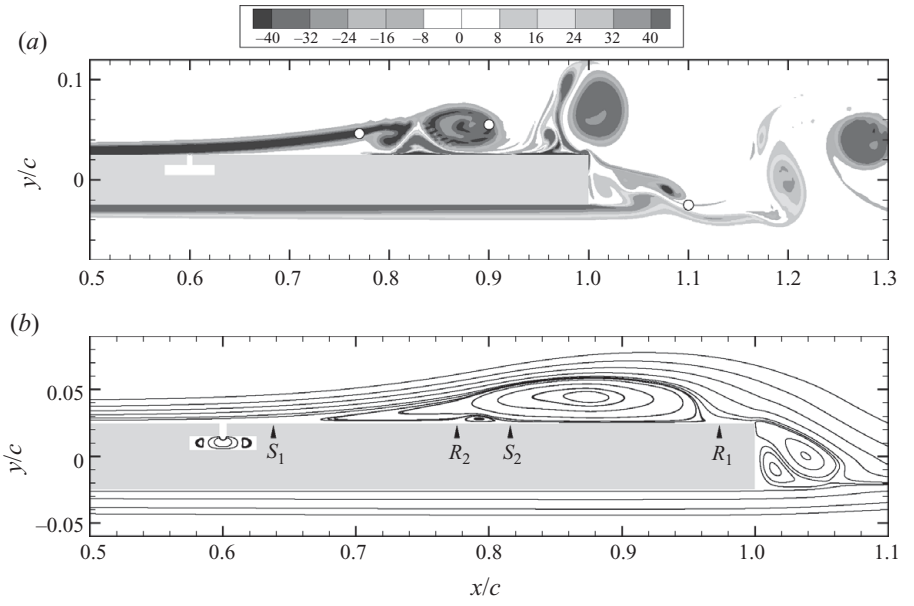

FIGURE 5. Baseline separated flow (Case 0) at $Re = 6 \times 10^4$ obtained from two-dimensional Navier–Stokes simulation on Grid II: (*a*) contours of instantaneous spanwise vorticity ($\omega_z c/U_\infty$) at $t = 20c/U_\infty$. The plot also shows 'probe' locations where the time series of cross-stream velocity v is recorded for spectral analysis. (*b*) Mean flow streamlines.

where $q = \rho U_\infty^2/2$ is the free-stream dynamic pressure, d is the SJ slot width and c is the chord length. The choice of $V_J = 0.1U_\infty$ fixed c_μ to a value of 1.3×10^{-4}. This value of c_μ is at least an order of magnitude lower than the lowest values used in the experiments of Seifert *et al.* (1993, 1996), Amitay *et al.* (1997) and Chatlynne *et al.* (2001). The simulations with SJ forcing are advanced for a total time of $15c/U_\infty$, of which the last 10 time units are used for the computation of time-mean flow statistics discussed in § 4.2.

Next, the simulations of the baseline separated flow and flows with SJ forcing are repeated at $Re = 1 \times 10^5$ to investigate the effect of the Reynolds number on the characteristic frequency scales and the response of the separated flow to SJ forcing at this higher Reynolds number. All other simulation parameters are held at the same values as in the simulations at $Re = 6 \times 10^4$. As before, the simulations at $Re = 1 \times 10^5$ are carried out on two different unstructured meshes to ascertain the grid independency of the simulation results. The nominal grid (Grid II), used in the $Re = 6 \times 10^4$ simulations, is employed as the baseline grid to start the simulations at $Re = 1 \times 10^5$ and is subsequently refined to yield a finer Grid III which is the nominal grid at this Reynolds number. The salient differences between these grids are summarized in table 1.

4. Results and discussion

4.1. *Baseline uncontrolled separated flow at* $Re = 6 \times 10^4$

4.1.1. *Vortex dynamics and mean flow characteristics*

Figure 5(*a*) shows the contours of instantaneous spanwise vorticity ($\omega_z c/U_\infty$) computed at $t = 20c/U_\infty$ on Grid II. The boundary-layer flow on the upper surface

Case	Grid	f_J/f^0_{lock}	$F^+_J = f_J c/U_\infty$	S_1	R_1	L_{sep}	H_{sep}
0	I	None	–	63.9	97.2	33.3	3.34
0	II	None	–	63.8	97.3	33.5	3.37
1	II	1/4	0.725	66.8	97.0	30.3	2.88
2	II	1/3	0.967	66.6	96.6	30.1	2.55
3	II	1/2	1.450	67.2	94.3	27.1	1.90
4	II	1	2.900	67.8	92.2	24.4	1.52
5	II	1.25	3.625	68.3	89.9	21.6	1.25
6	II	2	5.800	66.8	85.4	18.6	1.52
7	II	3	8.700	64.7	98.0	33.4	3.44
8	II	4	11.600	64.4	97.8	33.4	3.41

TABLE 2. Various cases simulated with SJ forcing of the baseline separated flow at $Re = 6 \times 10^4$ and $V_J/U_\infty = 0.1$. Also included are the locations and sizes of the mean separation bubble expressed as percentage of chord length c for these various cases.

of the airfoil loses momentum and thickens due to adverse pressure gradient induced by blowing and suction on the top boundary of the computational domain. Unable to overcome the pressure gradient, the retarded boundary-layer flow separates at $x/c = 0.638$. The inflection point that forms in the streamwise velocity profile at the separation point moves farther away from the wall with downstream development, resulting in an inviscid instability of the separated shear layer. As a consequence, the shear layer directly rolls up into large vortices. When these large vortices are of some size and strength, they pinch off from the shear layer and convect downstream and interact with Kármán vortex shedding in the wake. As these vortices convect, they entrain high-momentum fluid from the outer flow into the separated region close to the wall. This yields a closed aft-chord separation bubble in the mean as portrayed by the plot of mean streamlines shown in figure 5(*b*). Besides the distinct primary separation and reattachment points, S_1 and R_1, respectively, the mean separation bubble also shows secondary separation (S_2) and reattachment (R_2) of the reverse flow driven by the roll-up of large vortices in the separated region. The streamwise length of the mean separation bubble (L_{sep}) as measured from the primary separation point S_1 to the primary reattachment point R_1 is $0.335c$. The height of the mean separation bubble (H_{sep}), defined as the maximum cross-stream distance between the airfoil upper surface and the separating streamline (also called separatrix) is $0.0337c$. The streamwise locations of primary separation and reattachment points, their secondary counterparts, and the length and height of the mean separation bubble have been obtained from the simulations at $Re = 6 \times 10^4$ on Grids I and II (see table 2), and they show excellent agreement with one another with a variability of less than 1 % between them.

Figure 6(*a*) shows the comparison of mean pressure distribution $\langle C_p \rangle$ obtained from two-dimensional Navier–Stokes simulations of Case 0 at $Re = 6 \times 10^4$ on Grids I and II. In this study, the coefficient of pressure C_p is defined as

$$C_p = \frac{p - p_{ref}}{q_\infty}, \tag{4.1}$$

where p is the pressure on the airfoil surface, q_∞ is the free-stream dynamic pressure and p_{ref} is the reference pressure whose value is determined by requiring $C_p = 1$ at the stagnation point. The plot shows a suction peak near the leading edge caused by the acceleration of the flow around the elliptic section followed by a strong pressure

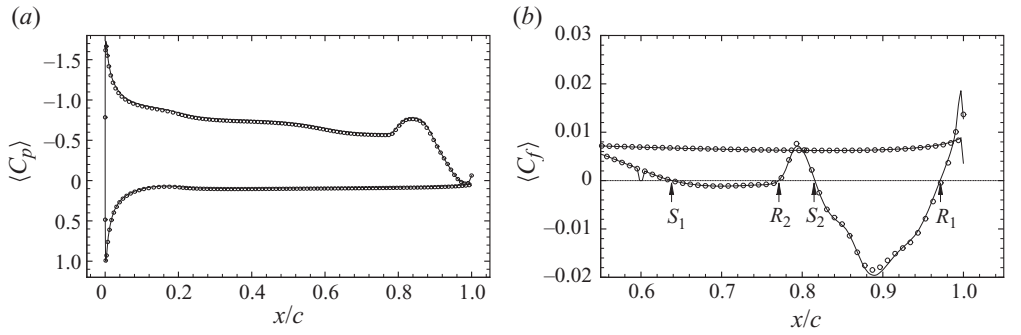

FIGURE 6. Comparison of surface pressure and local skin-friction distribution on the airfoil geometry obtained from two-dimensional Navier–Stokes simulations of Case 0 at $Re = 6 \times 10^4$ on Grids I and II: ——, Grid I; ○, Grid II.

recovery immediately downstream on the upper surface. The roll-up of the separated shear layer into large vortices is manifested by the existence of a local low pressure peak downstream of the plateau, followed by recovery to the value of base pressure acting on the trailing face. On the lower surface of the airfoil, a favourable pressure gradient exists over almost the entire length.

The distribution of streamwise local mean skin-friction coefficient $\langle C_f \rangle$ on the airfoil surface obtained for Case 0 on Grids I and II is plotted in figure 6(*b*). Throughout this study, the streamwise local skin-friction coefficient C_f is defined as

$$C_f = \frac{\tau_w}{q_\infty} = \mathrm{sgn}(u) \frac{\mu}{q_\infty} \left(\frac{\mathrm{d}|\boldsymbol{u}|}{\mathrm{d}n} \right)_{wall}, \tag{4.2}$$

where τ_w is the wall shear stress, q_∞ is the free-stream dynamic pressure, μ is the viscosity and $(\mathrm{d}|\boldsymbol{u}|/\mathrm{d}n)_{wall}$ is the normal derivative of the streamwise velocity magnitude at the wall. With this definition, the change in the sign of C_f from positive to negative and vice versa identifies locations of primary separation and reattachment, respectively, except for a narrow region between the leading edge and the stagnation point, wherein local streamwise direction of the attached flow is opposite in sense to x direction. Highest levels of skin friction that occur near the leading edge owing to local acceleration of the fluid around the elliptical section is not shown here. On the lower surface of the flat plate, the skin-friction distribution has almost a constant value. In the separated region on the upper surface, higher values of skin friction are distinctly seen to be associated with the airfoil surface, between S_2 and R_1, that is directly below the region of roll-up of the shear layer into large vortices. On the contrary, the separated region between S_1 and R_2 is associated with very low values of skin friction owing to the lower velocity of the recirculating fluid trapped in the dead-air region between the airfoil surface and the separated shear layer. A drop in C_f to zero value at $x = 0.6$ on the upper surface is an artefact arising from the presence of SJ slot that is left open to the external crossflow in the baseline uncontrolled simulations.

Figure 6 shows satisfactory grid convergence of the mean flow, particularly in the unsteady separated region. This indicates that the resolution employed in Grid II is reasonably satisfactory, and therefore we employ this grid for all of the subsequent simulations and analysis. A more comprehensive presentation of the grid dependency study for the baseline as well as forced flows can be found in Kotapati (2008).

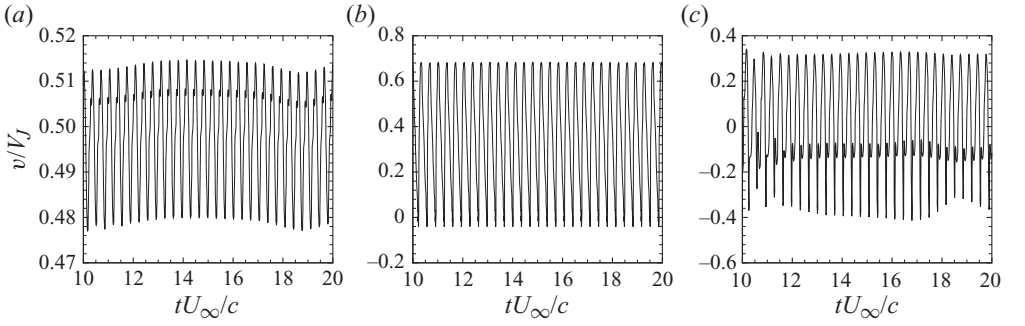

FIGURE 7. Temporal variations of cross-stream velocity v/U_∞ in (a) the shear layer, (b) the separation zone and (c) the wake for Case 0 at $Re = 6 \times 10^4$.

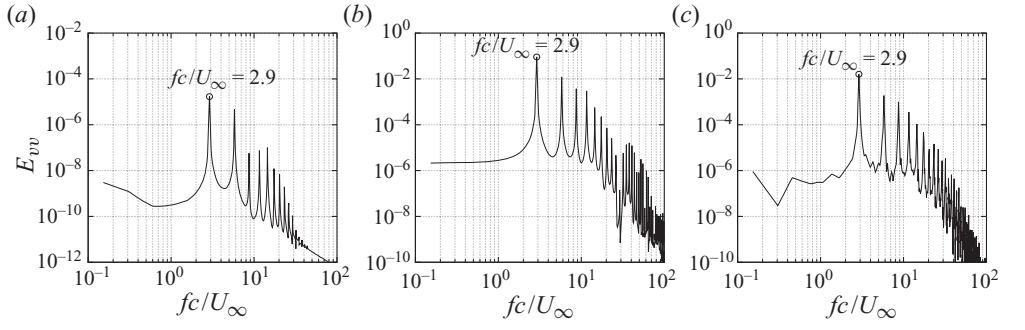

FIGURE 8. Power spectra corresponding to temporal variations of cross-stream velocity in (a) the shear layer, (b) the separation zone and (c) the wake for Case 0 at $Re = 6 \times 10^4$.

4.1.2. *Unsteady characteristics*

Time series of velocity components in the shear layer, separation zone and wake are recorded by probing the flow field at locations shown by open circles in figure 5(a). The temporal variations of cross-stream velocity v, at these probe locations is shown in figure 7(a–c). These temporal variations indicate that the flow field has reached a statistically stationary state in the time interval shown in these plots. The power spectra E_{vv} corresponding to these temporal variations are plotted in figure 8. Interestingly, the spectra indicate that the shear layer, the separation zone, and the wake are all locked on to a single frequency $f^0_{lock}c/U_\infty$ of around 2.9 corresponding to the dominant peak in these plots, i.e.

$$f^0_{lock} = f^0_{SL} = f^0_{sep} = f^0_{wake} \approx 2.9U_\infty/c.$$

In general, the presence of two or more basic frequencies (i.e. frequencies that are not harmonically related or integer multiples/fractions of one another) in high-Reynolds-number flows gives rise to sum and difference modes (Kourta *et al.* 1987) because of nonlinear interactions and results in a broadband spectrum. However, the present flow at $Re = 6 \times 10^4$ appears to be dominated by a global instability and so the spectra show one dominant peak at $fc/U_\infty = 2.9$ and several superharmonic peaks resulting from nonlinear interactions of this dominant mode with itself.

A number of questions arise regarding this lock-on state observed for the current case. Firstly, has the system locked on to this single frequency due to nonlinear

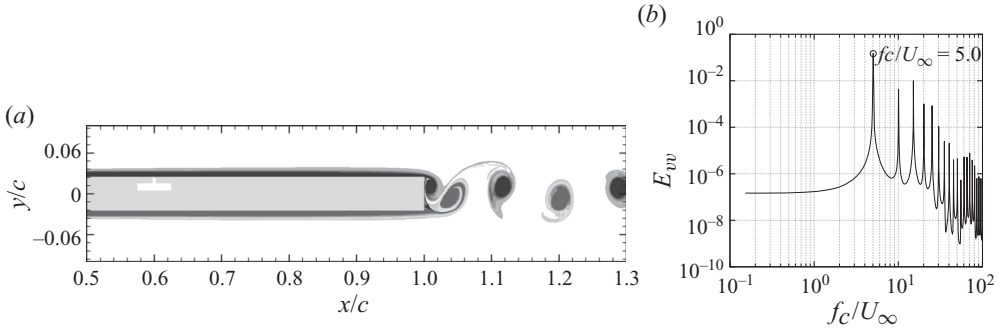

FIGURE 9. (*a*) Contours of instantaneous spanwise vorticity ($\omega_z c/U_\infty$) at $t = 20c/U_\infty$ (Contour levels are the same as in figure 5), and (*b*) power spectra corresponding to temporal variation of cross-stream velocity in the wake for unseparated flow (i.e. $\mathrm{d}p/\mathrm{d}x = 0$) at $Re = 6 \times 10^4$.

coupling mechanism or is this due to a coincidental match of the natural frequencies of the three constituents of this flow? Secondly, if the lock-on is indeed a result of nonlinear coupling, how does the system choose this particular frequency to lock-on to? Does the lock-on frequency correspond to the natural frequency of one of the constituents?

In order to gain further insight into these aspects of the flow we have carried out a simulation of flow past the flat plate 'without' a separation bubble, i.e. one in which the blowing–suction boundary condition at the top boundary of the computational domain is replaced by slip wall. This simulation allows us to determine the natural Kármán vortex shedding in the wake in the absence of the separation bubble. Figure 9(*a*) shows the contours of instantaneous spanwise vorticity for the case without the induced separation bubble and it clearly shows the presence of a typical Kármán vortex street in the wake of the plate. The power spectrum corresponding to the vertical component of velocity in the wake for this flow is shown in figure 9(*b*) and this indicates that $f^n_{wake} c/U_\infty \approx 5.0$. When this natural frequency is renormalized by the width of the wake W_{wake} (Roshko 1954), which for this flow is approximated by the plate thickness t, one obtains $f^n_{wake} W_{wake}/U_\infty \approx 0.25$. This is in line with the Strouhal number obtained for other bluff-body wakes. However the shedding frequency in the natural wake is obviously significantly removed from the system lock-on frequency of $f^0_{lock} c/U_\infty \approx 2.9$. Thus, the dynamics in the wake are clearly modified due to the presence of the separation bubble. Interestingly, however, renormalizing the wake vortex shedding frequency for Case 0 by the width of its wake $W_{wake} = t + H_{sep}$, we find that $f^0_{wake} W_{wake}/U_\infty \approx 0.24$, which is quite close to the value of 0.25 obtained for natural wake vortex shedding. On the other hand, renormalization of the lock-on frequency using the free-stream velocity U_∞ and the length of the recirculation bubble L_{sep} associated with the separated region of Case 0 yields $f^0_{sep} L_{sep}/U_\infty \approx 1$. It has been demonstrated by Seifert *et al.* (1996) that the most effective non-dimensional frequencies for forcing the separated region and increasing the lift are also $f L_{sep}/U_\infty \approx 1$, thereby implying that the dominant wavelength associated with the separated region is almost always comparable to the streamwise length L_{sep} requiring control. Thus, the final lock-on state consists of a separation bubble and wake that although locked onto the same frequency, also simultaneously indicate that they adhere to their natural frequency scalings. This also seems to imply that while the length of the separation bubble is primarily

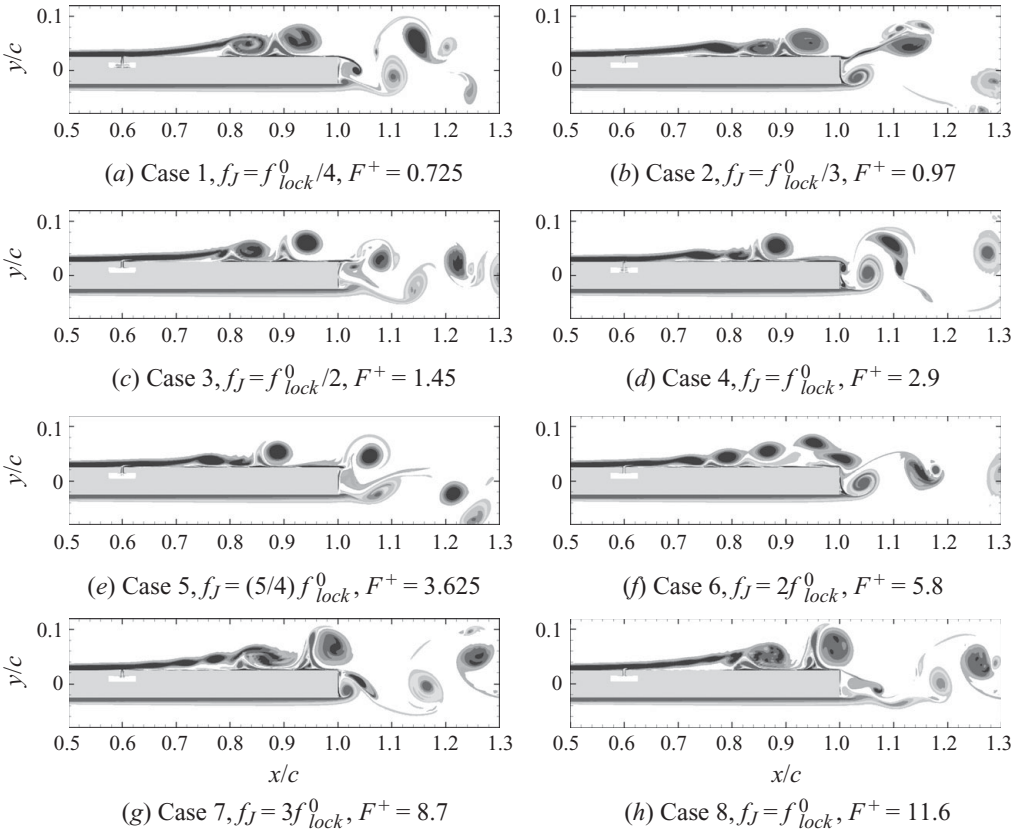

(*a*) Case 1, $f_J = f^0_{lock}/4$, $F^+ = 0.725$ (*b*) Case 2, $f_J = f^0_{lock}/3$, $F^+ = 0.97$

(*c*) Case 3, $f_J = f^0_{lock}/2$, $F^+ = 1.45$ (*d*) Case 4, $f_J = f^0_{lock}$, $F^+ = 2.9$

(*e*) Case 5, $f_J = (5/4) f^0_{lock}$, $F^+ = 3.625$ (*f*) Case 6, $f_J = 2f^0_{lock}$, $F^+ = 5.8$

(*g*) Case 7, $f_J = 3f^0_{lock}$, $F^+ = 8.7$ (*h*) Case 8, $f_J = f^0_{lock}$, $F^+ = 11.6$

FIGURE 10. Contours of instantaneous spanwise vorticity ($\omega_z c/U_\infty$) for Cases 1–8 at $Re = 6 \times 10^4$. Contours levels are the same as in figure 5.

determined by the dynamics of the separation bubble, its height, at least of this aft-chord separation case, is affected significantly by the wake dynamics. The shear layer, which can respond to frequencies in a broad range (Ho & Huerre 1984; Wu *et al.* 1998) seems to lock on to the frequency that is chosen by the coupling between the separation bubble and the wake.

4.2. *Synthetic jet forcing of the separated flow at* $Re = 6 \times 10^4$

In this section, the effect of forcing the baseline separated flow (Case 0) at $Re = 6 \times 10^4$ using an SJ actuator placed slightly upstream of the point of primary separation is examined. The SJ actuator has a slot of width $d = 0.0065c$, flush-mounted normal to the airfoil upper surface and centred at $x/c = 0.6$. The table 2 summarizes the different cases that result from forcing the SJ actuator at the lock-on frequency and some of its subharmonics and superharmonics.

4.2.1. *Vortex dynamics*

Figure 10(*a–h*) shows contour plots of instantaneous spanwise vorticity ($\omega_z c/U_\infty$) obtained from two-dimensional Navier–Stokes simulations of Cases 1–8 at $Re = 6 \times 10^4$ on Grid II. Based on these plots, the response of the flows to SJ forcing can be divided into three categories. The first category is the low-frequency response which is observed for $f_J/f^0_{lock} = 1/4$, $1/3$ and $1/2$. Comparing these cases with the unforced

flow (figure 5*a*), we note that the forcing seems to produce no noticeable change in the formation/evolution of the vortex structures in the separation bubble or the wake.

On the other end of the spectrum is the response of the flow to high-frequency perturbations which is characteristic of the cases with $f_J/f^0_{lock} = 2, 3$ and 4. The one commonality between these cases is that the vortices shed from the shear layer into the wake are quite large (larger than those for the unforced flow) and are formed by the merger of two or more vortices emanating from the shear layer. The separated shear layer for $f_J/f^0_{lock} = 2, 3$ also shows a distinct roll-up into Kelvin–Helmholtz (K–H) vortices whereas, for $f_J/f^0_{lock} = 4$, the vortices in the shear layer are less clearly formed. It should be noted that linear stability analysis of the mean flow for Case 0 carried out by Kotapati *et al.* (2007) indicates that the preferred frequency for the shear layer instability is $7.3U_\infty/c$. Thus it is not surprising that forcing the shear layer at close to these frequencies ($f_J c/U_\infty = 5.8$ and 8.7) leads to the formation of K–H vortices whereas forcing at a much higher frequency $f_J c/U_\infty = 11.6$ produces a diminished response. This issue is discussed in more detail when we examine the temporal response of the forced flow.

The third type of response is the one that is observed for Cases 4 and 5 ($f_J/f^0_{lock} = 1, 1.25$). For these two cases, we observe a significant flattening and reduction in size of the vortices formed at the downstream end of the shear layer. We also note that the separated shear layer stays closer to the plate surface and the release of vortices from the separation bubble also occurs slightly further upstream than all of the other cases.

4.3. *Mean flow characteristics*

Figure 11(*a–h*) shows mean streamlines obtained from two-dimensional Navier–Stokes simulations of Cases 1–8 at $Re = 6 \times 10^4$ on Grid II. As observed in the contour plots of instantaneous spanwise vorticity, mean streamlines show that forcing the shear layer between the first subharmonic and the first superharmonic of the lock-on frequency delays separation, and also reduces the length and height of the mean separation bubble. It is important to note that SJ forcing at the baseline lock-on frequency (Case 4) significantly reduces the size of the mean recirculation behind the blunt trailing face and this has some implications for the pressure field which will be discussed later. Of all the cases studied, Case 5 with forcing at $1.25f^0_{lock}$ shows the largest reduction in the streamwise extent of reverse flow. The streamline patterns corresponding to high-frequency forcing (Cases 7 and 8) indicate that the flow is essentially uncontrolled and appears very similar to the baseline separated flow.

The mean pressure distribution on the airfoil surface obtained from two-dimensional Navier–Stokes simulations of Cases 1–8 with SJ forcing is plotted in figure 12(*a*). Also included in these plots is the pressure distribution for the baseline separated flow of Case 0. SJ forcing of the separated flow at the baseline lock-on frequency (Case 4) modifies the pressure distribution over the entire airfoil surface, an effect that is probably associated with the noticeable reduction in the size of the mean recirculation bubble immediately behind the blunt trailing face (see figure 11*d*). With an increase in the forcing frequency from Cases 1–4, a monotonic reduction in the low-pressure peak and an increase in the rate of pressure recovery is noticed in the separated region. The rate of pressure recovery over the airfoil surface from which the boundary layer separates in the absence of control is a direct measure of the success of separation control (Seifert & Pack 1999), and as such, it can be used as a parameter in closed-loop ASC schemes. Case 5 with forcing at $F_J^+ = 3.625$ that resulted in the smallest mean separation bubble also has the highest rate of

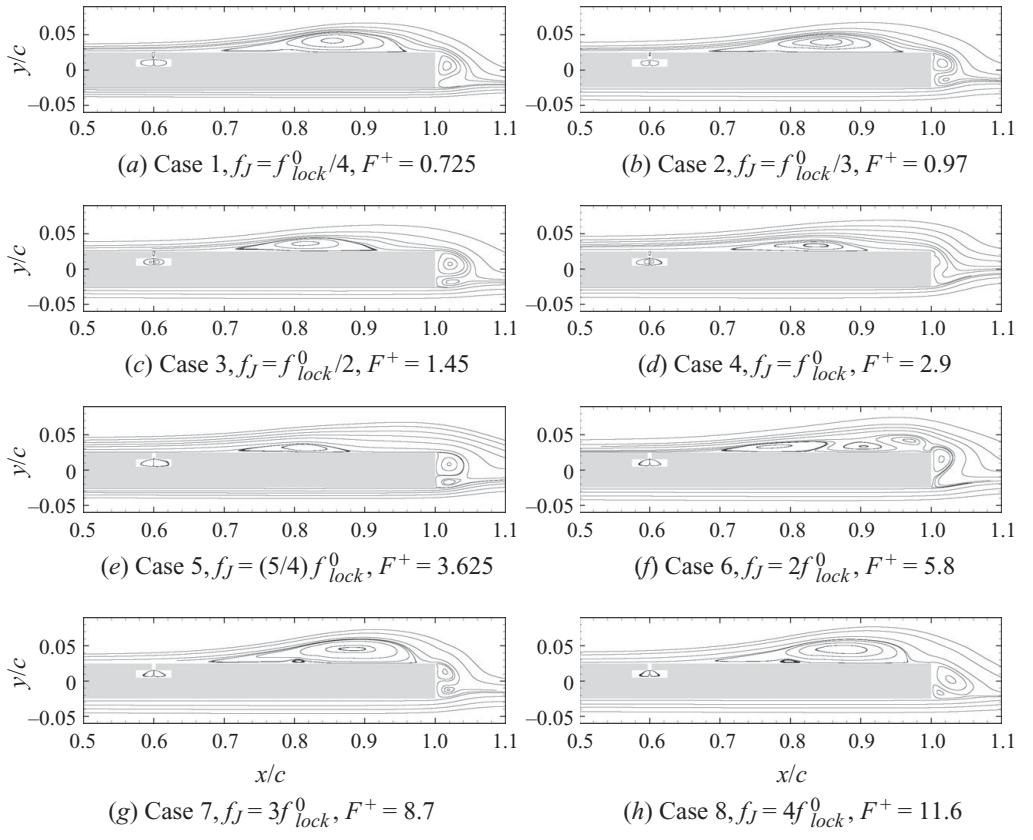

FIGURE 11. Mean streamlines for Cases 1–8 at $Re = 6 \times 10^4$.

pressure recovery in the separated region. Case 6 with forcing at $F_J^+ = 5.8$ shows the earliest pressure recovery downstream of the pressure plateau. However, this recovery decreases and forms a second plateau which is consistent with the development of a secondary separation bubble close to the trailing edge, as is evident in the mean streamline plot in figure 11(*f*). The apparent ineffectiveness of control at higher forcing frequencies (Cases 7 and 8) leaves the pressure distribution grossly unchanged as compared to the pressure distribution of Case 0.

Next, the distribution of mean skin-friction coefficient on the suction side of the airfoil surface for Cases 0–8 shown in figure 12(*b*) is examined. The streamwise locations of the primary separation and reattachment points for the time-mean flow, and the length of the mean separation bubble as measured by the distance between the primary separation and primary reattachment points are summarized in table 2. Also included is the maximum height of the mean separation bubble for Cases 1–8 determined by the streamline pattern for the mean flow. The table shows that with an increase in the forcing frequency from Cases 1–5, the length of the separated region, measured as the streamwise extent over which $\langle C_f \rangle < 0$, decreases monotonically. Lack of control effectiveness in Cases 7 and 8 leads to very little change in the skin-friction distribution as compared to the baseline separated flow.

Another means of assessing the effectiveness of the control and reduction in separation bubble size is to examine the displacement thickness δ^* of the flow for the various cases. In the current flow, we compute the displacement thickness for the

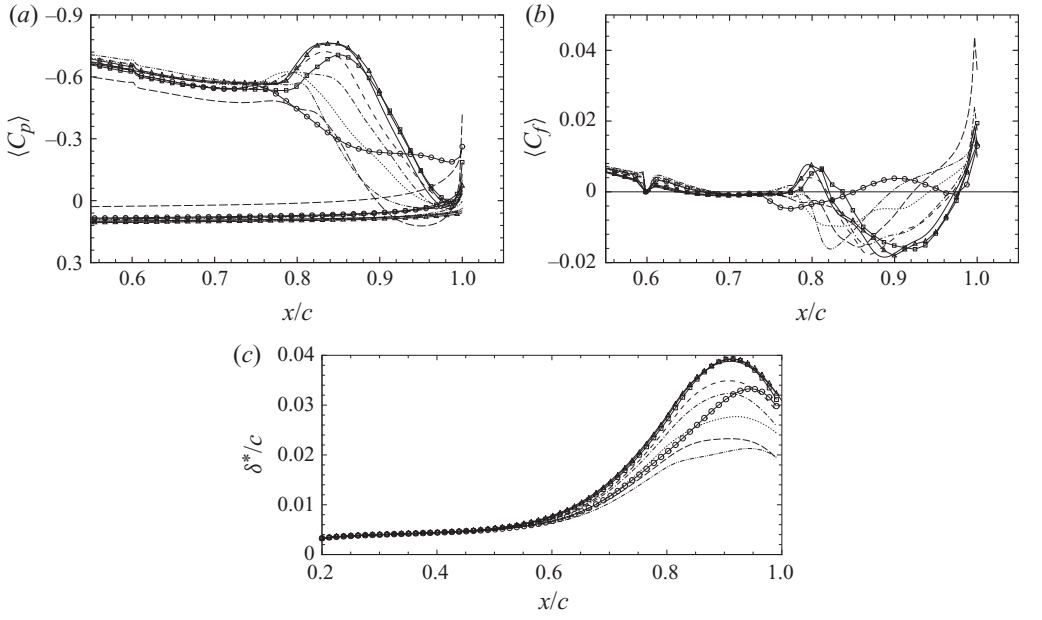

FIGURE 12. (*a*) Pressure $\langle C_p \rangle$, (*b*) skin-friction coefficient $\langle C_f \rangle$ and (*c*) displacement thickness δ^*, distribution on the airfoil surface for Cases 0–8 at $Re = 6 \times 10^4$. ——, Case 0 (no forcing); ----, Case 1 ($f_J = f^0_{lock}/4$); –·–, Case 2 ($f_J = f^0_{lock}/3$); ·····, Case 3 ($f_J = f^0_{lock}/2$); ––––, Case 4 ($f_J = f^0_{lock}$); –··–, Case 5 ($f_J = 5f^0_{lock}/4$); ○——○, Case 6 ($f_J = 2f^0_{lock}$); □—□, Case 7 ($f_J = 3f^0_{lock}$); △—△, Case 8 ($f_J = 4f^0_{lock}$).

mean flow as follows:

$$\delta^*(x) = \int_{y=y_{min}}^{y_{min}<y=y|_{u_e}\leqslant y_{max}} \left(1 - \frac{u(x)}{u_e(x)}\right) \mathrm{d}y, \tag{4.3}$$

where y_{min} is the y-coordinate on the airfoil surface, y_{max} is the y-coordinate where the streamwise velocity profile at the most downstream location on the flat plate (i.e. $x = c$) has its maximum, u_e is the boundary-layer edge velocity defined as $u_e(x) = \max\{u(x, y_{min} < y \leqslant y_{max})\}$, and $y|_{u_e}$ is the y-coordinate at which $u = u_e$. This redefiniton of the upper limit of the integrals from the standard form $y \to \infty$ is necessary because $u \neq U_\infty$ as $y \to \infty$ owing to the blowing–suction boundary condition applied at the top boundary.

The streamwise variation of the computed displacement thickness for Cases 0–8, is plotted in figure 12(*c*). In general, the larger the mean separation bubble, the larger is its displacement thickness. The separation bubble with smallest H_{sep}, resulting from SJ forcing at $F_J^+ = 3.625$ in Case 5, has the lowest displacement thickness in the separated region. Cases 7 and 8, for which the forced flow is essentially uncontrolled, have a very similar variation of displacement thickness as the baseline separated flow of Case 0.

4.4. *Temporal response and lock-on in forced flow*

Studying the temporal response of the flow to SJ forcing can provide further insight into the nonlinear interactions and the resulting vortex dynamics. We examine this response by extracting the temporal variation of velocity at three distinct locations in the flow on the upper surface of the plate. The locations are denoted by open circles in

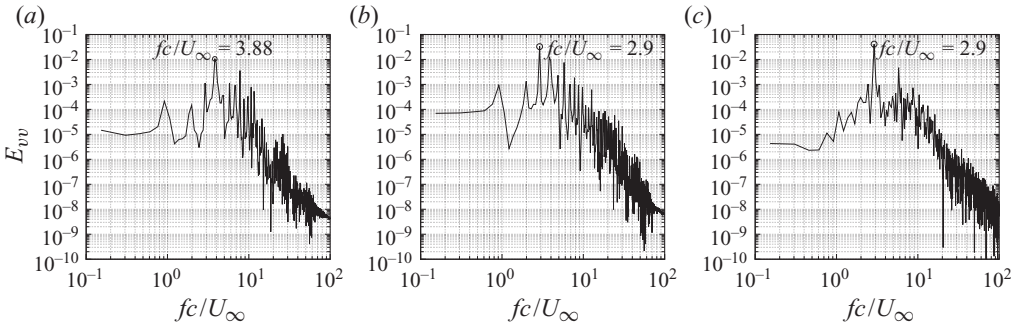

FIGURE 13. Power spectra corresponding to the temporal variations of cross-stream velocity in (*a*) the shear layer, (*b*) the separation zone and (*c*) the wake for Case 2 ($F_J^+ = 0.97$) at $Re = 6 \times 10^4$.

figure 5(*a*). The first location is in the shear layer downstream of the mean separation point but upstream of the locations where the vortices roll up into the separation bubble. The second point is at the downstream end of the separation bubble where vortices that roll up in the separation bubble are released. The third location is in the wake at a point which is vertically aligned with the lower surface of the plate. It should be noted that these three locations are to be considered representative of the shear layer, separation bubble and wake dynamics and as such, other locations in the local vicinity of these points also indicate similar behaviour.

We begin this analysis by focusing on the power spectra of the cross-stream velocity v for three cases, namely Cases 2, 5 and 8, in figures 13–15, respectively. These three cases are considered to be representative of the flow response to low, medium and high-frequency SJ forcing, and thus a detailed analysis of these cases sets the stage for us to describe the overall behaviour of the flow.

The spectrum in figure 13 corresponds to Case 2, for which $F_J^+ = 0.97$. The plots show that the separation bubble and wake do not respond to the low-frequency perturbation and continue to oscillate at the baseline lock-on frequency of $f^0_{lock} = 2.9U_\infty/c$. On the other hand, the shear layer responds by shifting its most energetic time scale to a frequency of $f^0_{SL} = 3.88U_\infty/c$ which is equal to $4F_J^+$. Thus for this low-frequency perturbation, the shear layer locks-on to a superharmonic of the forcing frequency. It should however be noted that while the perturbation provided is 1/3 of the natural lock-on frequency, the shear layer response is not at $3F_J^+$. This indicates a degree of decoupling of the shear layer dynamics from that of the separation bubble and the tendency of the shear layer to respond at frequencies that are closer to it natural frequency of $f^n_{SL}c/U_\infty \approx 7.3$. Also worth pointing out is the fact that despite the increase in the most energetic frequency of the shear layer, the separation bubble and wake maintain the response at the unforced lock-on frequency. This indicates that the shear layer has limited influence on the dynamics of the separation bubble and wake. The response of this case is representative of Cases 1 and 3 which are not discussed in detail here but the data for which is provided in the lock-on diagrams to be shown later.

Figure 14 shows the response of the flow for Case 5 for which $F_J^+ = 3.625$. This frequency is close to the system lock-on frequency of $2.9U_\infty/c$ and for this case, we find that all three flow constituents lock-on to the forcing frequency. A similar response is also observed for Case 4 where the system is forced at its natural lock-on

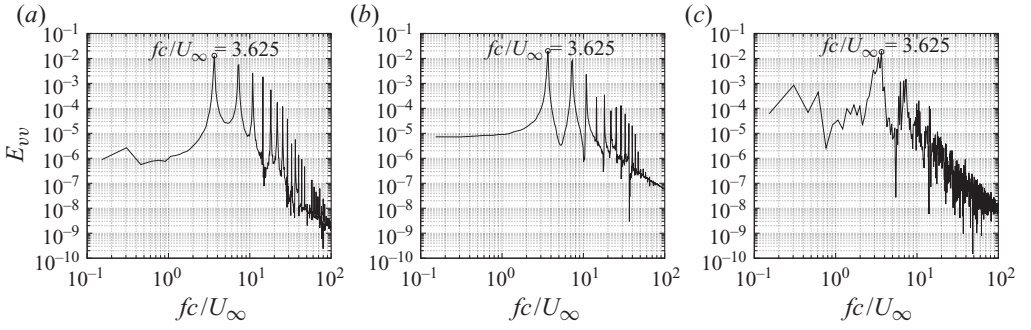

FIGURE 14. Same as figure 13 for Case 5 ($F_J^+ = 3.625$).

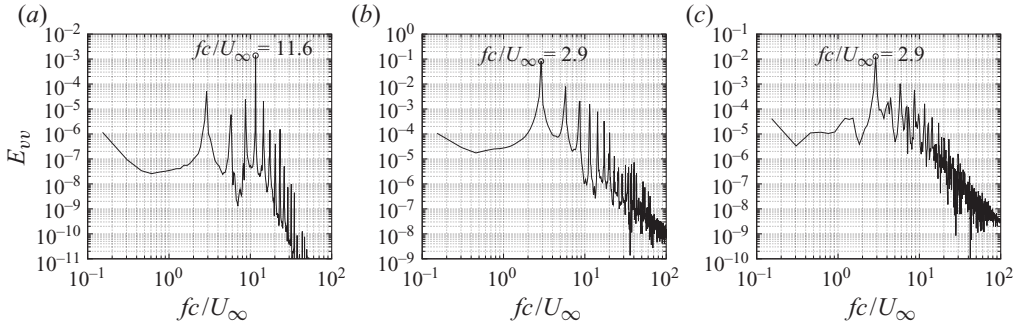

FIGURE 15. Same as figure 13 but for Case 8 ($F_J^+ = 11.6$).

frequency. Figure 15 shows the response of the flow for $F_J^+ = 11.6$ which is four times the natural lock-on frequency. For this case we find that the shear layer shows the largest response at the forcing frequency. This is despite the fact that the most unstable frequency of the shear layer as determined by linear stability theory in Kotapati (2008) is $f_{SL}^n c/U_\infty \approx 7.3$ which is substantially lower than forcing frequency. This confirms the notion that the shear layer can respond over a broad range of frequencies surrounding its own natural frequency. In contrast, the separation bubble and the wake revert to the natural lock-on frequency of $fc/U_\infty \approx 2.9$. This type of response wherein the shear layer locks onto the fundamental frequency of forcing and the separation bubble and wake retain their natural lock-on frequencies is also found for Cases 6–8.

The response observed for all the cases simulated in the current study are summarized in the frequency lock-on diagrams presented in figure 16. In addition to the eight forced cases described in detail in this section, we have also simulated six additional cases for the express purpose of filling different regions of the lock-on diagram. These cases have SJ frequencies corresponding to $F_J^+ = 2.175$, 2.5375, 3.48, 3.7, 4.35 and 6.525. In figure 16(a–c), the non-dimensional response frequencies in the shear layer, separated region and wake (denoted by f_{SL}^r, f_{sep}^r and f_{wake}^r, respectively) are plotted as functions of the non-dimensional forcing frequency using linear scales along the abscissa and the ordinate. These lock-on diagrams are also reformulated in terms of subharmonic and superharmonic of the natural lock-on and forcing frequencies

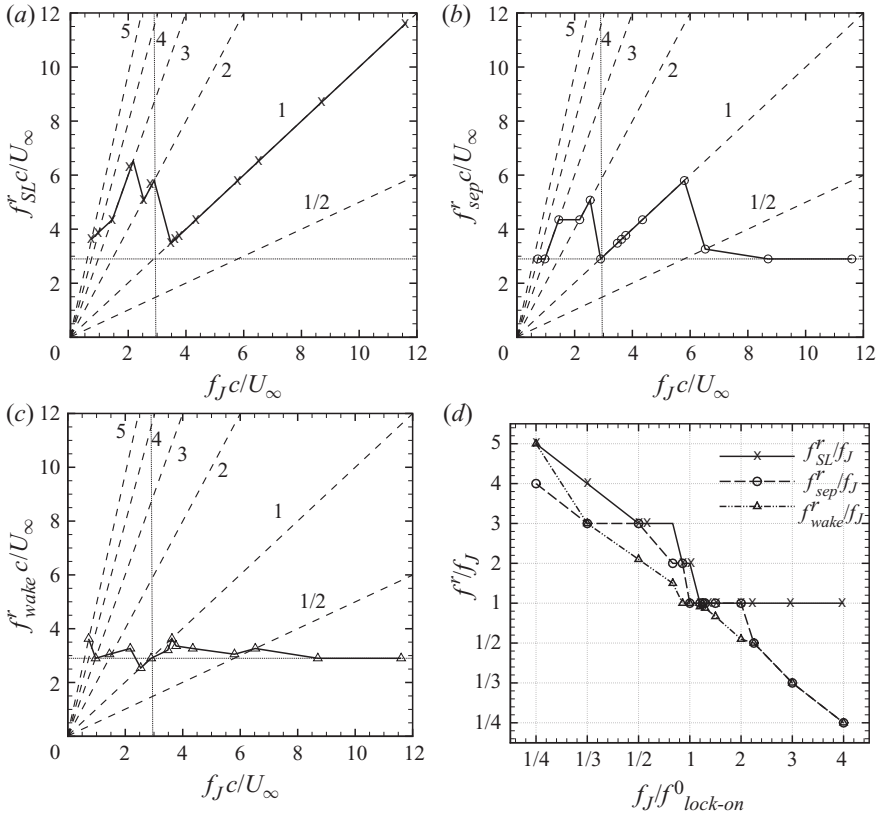

FIGURE 16. Frequency lock-on diagram for the forced cases at $Re = 6 \times 10^4$. Response of (*a*) shear layer, (*b*) separation bubble and (*c*) wake to SJ forcing at different frequencies. The horizontal and vertical dotted lines correspond to the natural lock-on frequency f^0_{lock}. The oblique dashed lines in these plots denote lock-on to subharmonic (1/2), harmonic (1) and superharmonics (2, 3, 4, 5) of the forcing frequency. (*d*) Lock-on plot for all three constituents expressed in terms of superharmonics and subharmonics.

and presented in figure 16(*d*). These plots indicate a number of interesting behaviours which are now described in detail.

Firstly, there are a number of regions in the forced response where one or more constituents of the flow lock-on to the fundamental forcing frequency, a situation we term as 'harmonic lock-on'. In particular, the shear layer shows the largest range of lock-on from $f_J = 1.25 f^0_{lock}$ to $4 f^0_{lock}$ which is the highest forcing frequency employed in the current study. The separation bubble shows the next largest region of harmonic lock-on from $f_J = f^0_{lock}$ to $2 f^0_{lock}$. Finally, the wake shows the smallest region of harmonic lock-on which extends from $f_J = 0.9 f^0_{lock}$ to $1.25 f^0_{lock}$. Interestingly, there is only a very small region centred around $f_J = 1.25 f^0_{lock}$ where all three constituents show a harmonic lock-on. The most obvious effect of such a perfect frequency lock-on in the forced flow is the absence of sum and difference modes owing to the presence of only one basic frequency in the system. This results in a well-organized vortical flow, as was also observed previously by Wu *et al.* (1998).

It is also interesting that whereas the unforced flow exhibits lock-on of all three constituents at f^0_{lock}, the lock-on for the forced flow occurs at $1.25 f^0_{lock}$. In fact, forcing at $f_J = f^0_{lock}$ leads to a situation where the wake and separation bubble lock on to the

forcing frequency whereas the shear layer shifts its response to the first superhamonic of the forcing frequency, i.e. $2f_J$. This by no means violates the flow physics since the perturbation being provided by the SJ is not infinitesimal and the nonlinear interaction allows the system to jump to a different lock-on state despite the fact that the forcing frequency is the same as the natural lock-on frequency.

In addition to the small region where all three constituents of the forced flow exhibit harmonic lock-on, there are regions where only two constituents concurrently show harmonic lock-on. For instance, in the region from $f_J = f^0_{lock}$ to $1.25f^0_{lock}$, both the separation bubble and the wake show harmonic lock-on whereas in the region from $f_J = 1.25f^0_{lock}$ to $2f^0_{lock}$, the shear layer as well as the separation bubble show harmonic lock-on. For high-frequency forcing, the flow also exhibits a range beyond $f_J = 2f^0_{lock}$ where only the shear layer exhibits harmonic lock-on whereas both the separation bubble and wake revert to the undisturbed lock-on frequency. Locking-in of the shear layer to the forcing frequency for high-frequency forcing at $f_J = 3f^0_{lock}$ and $4f^0_{lock}$ (Cases 7 and 8) leads to the amplification of K–H type instabilities and subsequent roll-up of the shear layer into discrete vortices. Since the forcing frequency at which the shear layer undergoes discretization is now at least twice as large as the baseline lock-on state that continues to persist in the separated region, the shear layer vortices undergo subharmonic pairing in order to reduce their characteristic frequency to that imposed by the separated region. Given the separation in the time scales of the shear layer and the separation bubble, the coalescence of small vortices into larger ones takes place in an almost stationary manner, setting up a strong localized reverse flow that further deteriorates the separated region and rendering SJ forcing ineffective. However, as discussed by Wu *et al.* (1998), these large vortices formed by the coalescence of smaller K–H type vortices can be used beneficially to enhance lift on post-stall airfoils as these lifting vortices carry more favourable circulation above the airfoil surface with a low-pressure core than even attached boundary layers at such high angles of attack. A final note regarding the high-frequency forcing is that both the separation bubble and the wake show a tendency to lock on to the subharmonic of the forcing frequency ($1/3f_J$ and $1/4f_J$ for Cases 7 and 8, respectively). In keeping with the terminology used here, this can be termed as 'subharmonic lock-on'.

The response at forcing frequencies below the natural lock-on frequency is considerably more complicated. Whereas the wake seems to decouple from the forcing frequency and lock on to its unforced shedding frequency of f^0_{lock}, the separation bubble and shear layer lock on to the superharmonics of the forcing frequency, a state we term as 'superharmonic lock-on'. In particular, the forcing frequency $f_J = (f^0_{lock}, f^0_{lock}/2, f^0_{lock}/3, f^0_{lock}/4)$ maps to shear layer response $f_{SL} = (2f_J, 3f_J, 4f_J, 5f_J)$ respectively. Given the relatively high natural frequency of the shear layer, the tendency of the shear layer to lock-on to high superharmonics of low forcing frequencies is not surprising. For low-frequency forcing, the resulting shear layer frequency is always less than twice the frequency of the separated region. This means that discrete vortices (if any) resulting from the amplification of K–H instability in the shear layer do not undergo subharmonic pairing as they convect downstream. Instead, the shear layer either directly rolls up into large vortices in the separated region or undergoes discretization into small vortices whose wavelength increases (frequency decreases) to a value imposed by the separated region as they convect downstream. These dynamic effects are consistent with the vortex dynamics observed in figure 10(*a–c*) and with previous observations of Seifert *et al.* (1996) in airfoil flows.

Thus the primary conclusion from examining the temporal response is that the flow does not respond in a smooth and continuous manner to forcing at different

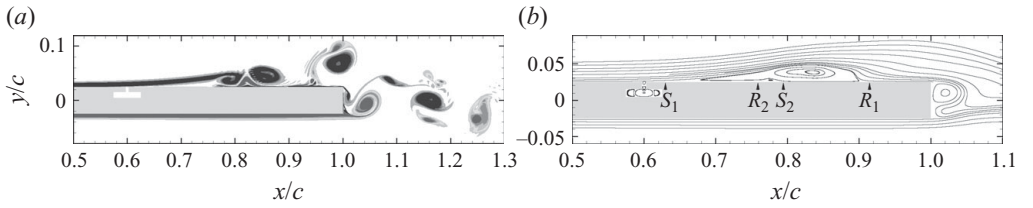

FIGURE 17. Baseline separated flow (Case 0) at $Re = 1 \times 10^5$ obtained from two-dimensional Navier–Stokes simulation on Grid III: (*a*) contours of instantaneous spanwise vorticity ($\omega_z c/U_\infty$) at $t = 20c/U_\infty$. Contours levels are the same as in figure 5. (*b*) Mean flow streamlines.

frequencies. Instead the response is characterized by the appearance of well-defined and distinct subharmonic, harmonic and superharmonic lock-on states. While the final state of the flow is determined by complex nonlinear interactions between the constituents of the flow, the linear response of each constituent also has some influence on this final state. Thus, for instance, the receptivity of the shear layer to high-frequency forcing is directly related to its linear response which naturally occurs at high frequencies. Similarly, the wake tends to have a limited response to SJ perturbations and is governed primarily by its own global instability mechanism.

5. Effects of the Reynolds number

The Reynolds number is one of the key parameters in this flow. Whereas the natural frequency of the shear layer depends directly on the Reynolds number, this is not the case for the separation bubble and the wake, and therefore changing the Reynolds number should have an effect on the lock-on phenomena observed in this flow. As such we have carried out an additional set of simulations at a significantly higher Reynolds number of 1×10^5. The objective of these simulations is to examine the extent to which the general observations made regarding the temporal response of this flow at the lower Reynolds number are valid for this higher Reynolds number. Both unforced and forced flow configurations are computed at this Reynolds number and the key observations are described briefly. Simulations at this Reynolds number were carried out on Grids II and III. The salient results were found to be quite insensitive to the grid and the results shown here correspond to Grid III.

Figure 17 shows contours of instantaneous spanwise vorticity ($\omega_z c/U_\infty$) at $t = 20c/U_\infty$ and mean streamlines for the uncontrolled separated flow (Case 0) at $Re_c = 1 \times 10^5$. The flow field at this higher Reynolds number appears qualitatively very similar to that at $Re_c = 6 \times 10^4$, with the separated shear layer directly rolling up into large vortices without any subharmonic pairing of smaller vortices. The resulting closed mean separation bubble shows distinct primary separation and reattachment points (S_1 and R_1) as well as secondary separation and reattachment points (S_2 and R_2) induced by vortex roll-up. The location and size of the mean separation bubble obtained for this Case 0 on Grid III is shown in table 3. In general, the separation point on a continuous surface moves downstream with increase in Re_c owing to increased inertia. However, a comparison of the data for Case 0 in table 3 with those obtained at $Re_c = 6 \times 10^4$ (see table 2) indicates that, with the chosen flow configuration, fixing the amplitude and the cross-stream distance of the blowing–suction velocity profile from the airfoil surface to the same values while only increasing Re_c induces earlier suction leading to slightly earlier separation. Notwithstanding this earlier separation, the length and the height of the mean separation bubble reduce by 15 % and 30 %,

Case	f_J/f^0_{lock}	$F^+_J = f_J c/U_\infty$	S_1	R_1	L_{sep}	H_{sep}
0	None	–	63.0	91.6	28.6	2.35
1	1/4	0.95	67.9	90.9	23.0	1.07
2	1/3	1.27	67.9	90.5	22.6	0.91
3	1/2	1.9	68.2	88.2	19.9	0.78
4	1	3.8	68.8	84.2	15.4	0.55
5	2	7.6	69.0	83.9	14.9	0.53
6	3	11.4	64.2	93.1	28.9	2.44
7	4	15.2	63.7	91.9	28.2	2.34

TABLE 3. Various cases with ZNMF forcing of the baseline separated flow at $Re_c = 1 \times 10^5$ and $V_J/U_\infty = 0.1$. Also included are the locations and sizes of the mean separation bubble expressed as percentage of chord length c for these various cases computed on Grid III.

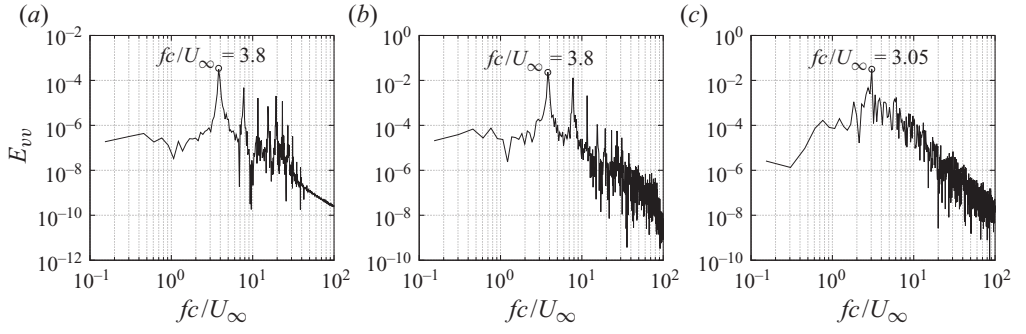

FIGURE 18. Power spectra corresponding to temporal variations of cross-stream velocity in (*a*) the shear layer, (*b*) the separation zone and (*c*) the wake from simulation of Case 0 at $Re_c = 1 \times 10^5$.

respectively, as Re_c increases from 6×10^4 to 1×10^5. This reduction in the size of the mean separation bubble with increase in Re_c is attributed to the decrease in displacement and momentum thicknesses of the shear layer that rolls up to form large vortices which in turn define the extent of the separated region.

The power spectra corresponding to temporal variations of the cross-stream velocity v in the shear layer, the separated region, and the wake obtained for Case 0 at $Re_c = 1 \times 10^5$ on Grid III are shown in figure 18. While the spectra for Case 0 at $Re_c = 6 \times 10^4$ indicated that the entire system was locked on to a single frequency, the spectra at $Re_c = 1 \times 10^5$ indicate that while the shear layer and separation region show lock-on, the wake shedding is not locked on to either one of them. This difference from the $Re_c = 6 \times 10^4$ case is likely due to the fact that in this higher Reynolds number case, the separation bubble closes further upstream of the wake and therefore the separation bubble does not get influenced by the wake to the same extent as it does for the previous case. From the spectra in figure 18, one determines

$$f^0_{lock} = f^0_{SL} = f^0_{sep} = 3.8U_\infty/c \quad \text{and} \quad f^0_{wake} = 3.05U_\infty/c.$$

Renormalizing the frequency f^0_{sep} by the characteristic length L_{sep} of its mean separation bubble yields $f^0_{sep}L_{sep}/U_\infty \approx 1$, again confirming that f_{sep} scales with the characteristic length of the separation bubble. Similarly, when the wake vortex shedding frequency for Case 0 is renormalized by the wake width $W_{wake} = t + H_{sep}$,

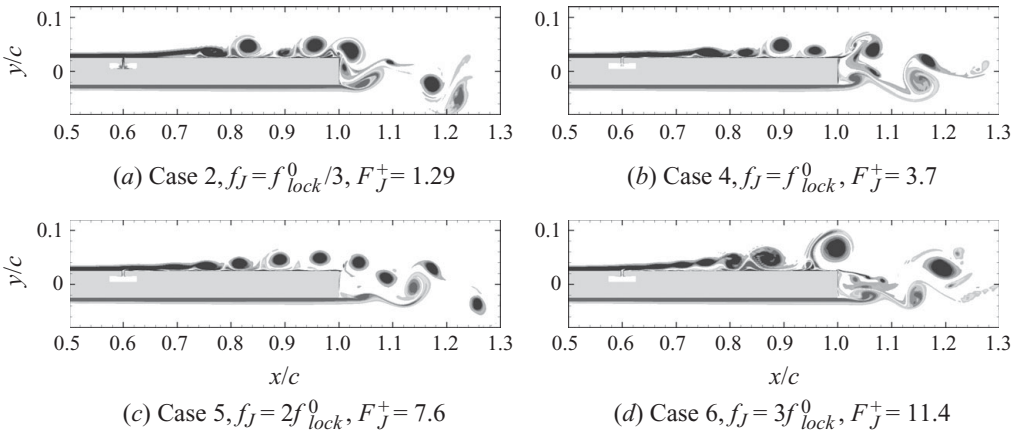

(*a*) Case 2, $f_J = f^0_{lock}/3$, $F^+_J = 1.29$ (*b*) Case 4, $f_J = f^0_{lock}$, $F^+_J = 3.7$

(*c*) Case 5, $f_J = 2f^0_{lock}$, $F^+_J = 7.6$ (*d*) Case 6, $f_J = 3f^0_{lock}$, $F^+_J = 11.4$

FIGURE 19. Contours of instantaneous spanwise vorticity ($\omega_z c/U_\infty$) for selected cases at $Re_c = 1 \times 10^5$. Contours levels are the same as figure 5.

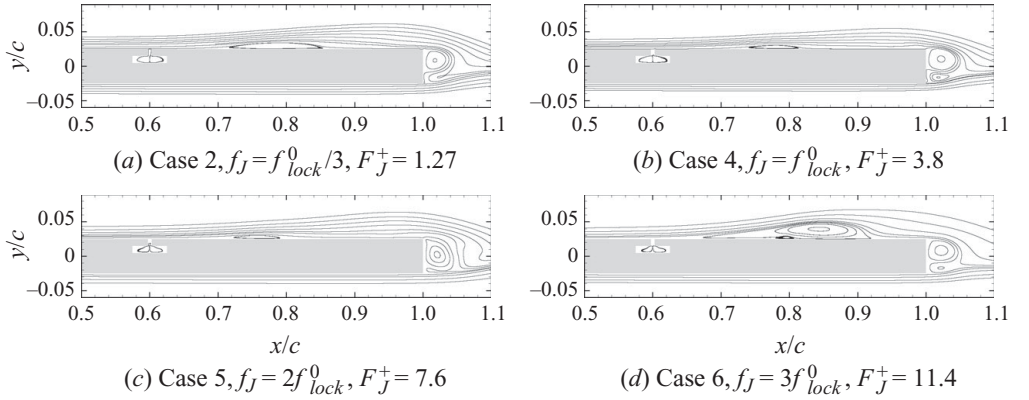

(*a*) Case 2, $f_J = f^0_{lock}/3$, $F^+_J = 1.27$ (*b*) Case 4, $f_J = f^0_{lock}$, $F^+_J = 3.8$

(*c*) Case 5, $f_J = 2f^0_{lock}$, $F^+_J = 7.6$ (*d*) Case 6, $f_J = 3f^0_{lock}$, $F^+_J = 11.4$

FIGURE 20. Mean streamlines for selected cases at $Re_c = 1 \times 10^5$.

one finds that $f^0_{wake} W_{wake}/U_\infty \approx 0.22$. This value closely agrees with the value of 0.24 obtained for $Re_c = 6 \times 10^4$, indicating that the simple definition of the characteristic width as $W_{wake} = t + H_{sep}$ works quite well for the current flow.

The uncontrolled baseline separated flow at $Re_c = 1 \times 10^5$ is now subjected to SJ forcing at the frequencies indicated in table 3. Figure 19(*a–d*) shows contours of instantaneous spanwise vorticity obtained for some selected cases on Grid III at $t = 35c/U_\infty$. The vortex dynamics at this higher Re_c is qualitatively very similar to that at $Re_c = 6 \times 10^4$, with the separated shear layer responding favourably to SJ forcing in Cases 1–5. In particular, SJ forcing in Cases 4 and 5 result in a train of evenly spaced vortices close to wall that continuously sweep the low-momentum fluid off the surface and enhance mixing with the outer flow. On the other hand, as previously observed at $Re_c = 6 \times 10^4$, forcing at $f_J \geqslant 3f^0_{lock}$ in Case 6 (as well as Case 7 not shown in the figure) essentially leaves the flow uncontrolled because of subharmonic pairing of K–H type vortices in the separated shear layer.

Mean streamlines obtained at $Re_c = 1 \times 10^5$ on Grid III are plotted for some selected cases in figure 20(*a–d*). In going from Case 1 to Case 5, the size of the mean separation bubble diminishes monotonically with increase in the forcing frequency.

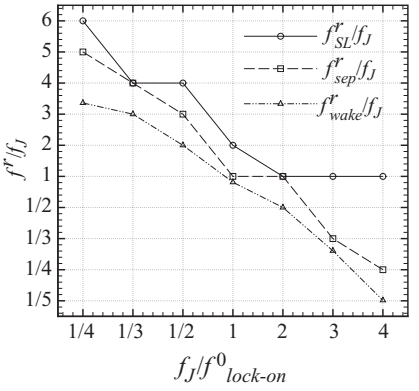

FIGURE 21. Frequency lock-on diagram for the forced cases at $Re = 1 \times 10^5$.

However, streamlines for Case 6 (as well as Case 7 not shown here) indicate that SJ forcing in these cases is ineffective, resulting in a similar separation bubble as in Case 0, complete with secondary separation induced by the reverse flow. The location and size of the mean separation bubble obtained for Cases 1–7 at $Re_c = 1 \times 10^5$ are summarized in table 3.

As with the previous case, we have examined the frequency spectra in the various regions of this flow to determine the response frequencies for the shear layer, separation region and the wake. Figure 21 shows the lock-on map constructed from these spectra and we can see immediately that the overall behaviour has similarities to the previous case. At high forcing frequencies, the shear layer locks on to the forcing frequency itself whereas the separation bubble and wake do not. In fact, the wake again shows evidence of subharmonic lock-on by locking on to (1/5)th of the forcing frequency when the forcing frequency is $4f^0_{lock}$. There is a range that at least extends between $f_J = f^0_{lock}$ and $f_J = 2f^0_{lock}$ where the separation bubble locks on to the forcing frequency, and it is at the higher end of this range that the maximum reduction in separation is observed. At lower forcing frequencies, both the separation bubble and the shear layer lock on to the superharmonics of the forcing frequency. Note that as before, the tendency of the separation bubble and the shear layer is to select high superharmonics such that their response frequency ends up being higher than f^0_{lock}. For instance, for forcing at $1/2f^0_{lock}$ and $1/4f^0_{lock}$ the shear layer locks on to $4f_J$, and $6f_J$, respectively. Similarly, for forcing at $1/2f^0_{lock}$, $1/3f^0_{lock}$ and $1/4f^0_{lock}$ the separation bubble locks on to $3f_J$, $4f_J$ and $5f_J$, respectively. In the case of the shear layer, this is clearly due to the fact that the natural frequency of the shear layer is significantly higher than f^0_{lock} and thus the forced shear layer naturally locks on to higher frequencies if possible. In the case of the separation bubble, the lock-on to high frequencies is at least partially tied to the fact that the forcing tends to reduce the length scale of separation bubble which decreases the time scale of this constituent of the flow. The fact that the lock-on states are much more dramatic for the lower Reynolds number is probably because of the smaller scale separation between the various components at this Reynolds number than at the higher Reynolds number. As the Reynolds number is increased, the time scale associated with the shear layer decreases whereas the time scales associated with the separation bubble and the wake stay relatively independent of the Reynolds number. Thus the scale separation between the shear layer and the other two components increases for fixed separation bubble size and location. This would tend to modify, and in some cases mitigate these lock-on phenomena.

6. Conclusions

A novel flow configuration has been proposed to investigate SJ-based separation control in canonical separated airfoil flows. These flows are generally characterized by distinct frequency scales corresponding to the shear layer instability f_{SL}, the unsteadiness in the separated region f_{sep} and the vortex shedding in the wake f_{wake}. The proposed configuration attempts to reproduce this behaviour in a simpler more easily studied flow. In this configuration, separation is induced on the upper surface of a flat plate with an elliptic leading edge and a blunt trailing edge, by inducing an adverse pressure gradient on the top surface of the plate. Unlike an actual airfoil, the current configuration allows prescription of the location and extent of the separation bubble in a manner which is fairly independent of parameters such as AOA and the Reynolds number. This allows us to study the nonlinear dynamics of separated airfoil flows in a way that eliminates many confounding variables.

Highly resolved two-dimensional Navier–Stokes simulations have been carried out for this canonical separated flow with the focus being on studying the dynamics of aft-chord separation. The effect of the forcing frequency on the associated separation control is studied systematically in order to determine the effective frequencies for SJ forcing and the nonlinear interactions between the various constituents of this flow. Simulations of the baseline uncontrolled flow for this particular case at a chord Reynolds number Re_c of 6×10^4 indicate that the entire system, comprising of the shear layer, the separation zone and the wake, is locked on to a single frequency of $f^0_{lock}c/U_\infty = 2.9$. In this separated flow, it was found that $f^0_{sep}L_{sep}/U_\infty \approx 1$, where L_{sep} is the characteristic length of the mean separation bubble, and $f^0_{wake}W_{wake}/U_\infty \approx 0.24$, where W_{wake} is the characteristic width of the wake. Kotapati (2008) used linear stability analysis of the mean flow to estimate the natural frequency of the shear layer to be $7.3U_\infty/c$, whereas the natural wake frequency (in the absence of the separation bubble) was determined to be $5.0U_\infty/c$. The fact that the separated flow locks on to a frequency corresponding to $2.9U_\infty/c$, clearly demonstrates that nonlinear interactions play a crucial role in determining the dynamics of this flow.

The separated flow at $Re_c = 6 \times 10^4$ is subjected to periodic forcing in the region slightly upstream of the separation point using an SJ actuator embedded on the airfoil upper surface. The forcing frequencies cover a range from one-forth to four times the baseline lock-on frequency f^0_{lock}. Spectral analysis of the forced flow shows that the flow does not respond in a smooth and continuous manner with variation in the forcing frequency. Instead, the response is characterized by the appearance of distinct lock-on states in the three constituents of the flow. These lock-on states usually involve one or more constituents of the flow locking onto either the forcing frequency or its subharmonics or superharmonics. Thus, a number of different lock-on states can be found for the forced flow. It should be noted that while the final state of the flow is determined by complex nonlinear interactions between the flow constituents, the linear response of each constituent also has some influence on this final state. Thus, for instance, the receptivity of the shear layer to high-frequency forcing is directly related to its linear response which naturally occurs at high frequencies. Similarly, the wake tends to have a limited response to SJ perturbations and is governed primarily by its own global instability mechanism. Simulations of both the unforced and forced flow conducted at a higher Reynolds number of 1×10^5 indicate similar lock-on regimes. However, given the variety of lock-on states available to this flow, the flow at these two Reynolds numbers do not show exactly the same lock-on states at similar forcing frequencies. The conclusion in this regard is that although the Reynolds

number modulates the lock-on behaviour (as expected), the general tendency of the flow to exhibit well-defined lock-on states remains unchanged.

At both Reynolds numbers, the most effective separation control, as measured by the extent of the mean separation bubble, occurs at the highest forcing frequency for which both the shear layer and the separated region are able to lock on to the fundamental forcing frequency. Note that although for the current flows, the most effective lock-on frequency ranged from $1.75 f^0_{lock}$ to $2.0 f^0_{lock}$, there is no reason to expect that this range could not be larger for different flows. In the current study, high-frequency forcing results in the formation of a train of K–H vortices which undergo vortex merger to form a large separation bubble vortex which renders the SJ forcing ineffective and sometimes even counter productive.

The current study provides insights that have clear implications for active control of separated airfoil flows. It is found that (i) the nonlinear interactions play a key role in determining the final stationary state of these flows; (ii) the stationary state usually involves some type of lock-on between one or more constituents of the flow; (iii) the variation in any governing parameter of the flow (which may include the Reynolds number, the location and size of separation as well as the forcing frequency) can lead to the flow jumping from one lock-on state to another; (iv) the objective of separation control therefore should be to make the system jump from its natural lock-on state to one that is most desirable (from the view of reduced separation), and do so with the least amount of input energy.

A number of caveats regarding the study need to be kept in mind. Firstly, the simulations are two-dimensional and therefore three-dimensional effects, including turbulence are not included. A limited set of three-dimensional large-eddy simulations of the same flow (Kotapati 2008; Kotapati *et al.* 2008) however indicate that the essential nonlinear dynamics of the two-dimensional flow are retained even in the presence of three dimensionality. Furthermore, experiments (which include three-dimensional effects) with an actual airfoil at $Re = 1 \times 10^5$ by Tian, Cattafesta & Mittal (2006) also show the presence of nonlinear coupling between the shear layer and the separated wake region. Despite this experimental and computational evidence, it is possible that three-dimensionality could modulate the nonlinear interactions between the different constituents of the flow in ways that are not apparent in a two-dimensional study. Secondly, although we have attempted to cover a wide range of forcing frequencies, the frequency range, especially on the high end, is limited by the expense of these simulations. It is possible that there are other effects (such as virtual aero-shaping) that might appear at much higher frequencies. Similarly, we have limited ourselves to one actuator location (with respect to the separation point) and one location of the separation bubble. Thus, many more configurations are possible and indeed worth investigating since they represent different types of flow separations. Some of the above configurations and effects can be investigated using simulations but experiments probably offer the most practical way of addressing these effects in a comprehensive manner. Finally, while the current configuration does serve as a useful canonical model of separated airfoil flows, there are some clear differences between the two configurations. Thus, it is highly desirable that the studies of this canonical configuration be augmented by studies of actual airfoil flows.

This work was supported by AFOSR under Grant F49550-05-1-0169 for R. Mittal and FA9550-05-0093 for L. N. Cattafesta. R. Mittal and R. B. Kotapati also acknowledge support from the Centre for Turbulence Research through the 2006 CTR Summer Programme and the use of CTR's CDP code for the numerical simulations.

REFERENCES

Amitay, M., Honohan, A., Trautman, M. & Glezer, A. 1997 Modification of the aerodynamic characteristics of bluff bodies using fluidic actuators. *Paper* 97-2004. AIAA.

Auld, R. & Mittal, R. 1999 Numerical simulation of flow past a wall-mounted flap. In *Bulletin of the American Physical Society*, Division of Fluid Dynamics Meeting 21–23 November 1999, New Orleans, LA. APS.

Bar-Sever, A. 1989 Separation control on an airfoil by periodic forcing. *AIAA J.* **27**, 820–821.

Bragg, M. B., Hienrich, D. C., Ballow, F. A. & Zaman, K. B. M. Q. 1996 Flow oscillation over an airfoil near stall. *AIAA J.* **34**, 199–201.

Bragg, M. B., Hienrich, D. C. & Khodadoust, A. 1993 Low frequency flow oscillation over airfoils near stall. *AIAA J.* **31**, 1341–1343.

Broeren, A. P. & Bragg, M. B. 1998 Low frequency flow field unsteadiness during airfoil stall and influence of stall type. *Paper* 98-2517. AIAA.

Chang, P. K. 1976 *Control of Separation*. McGraw-Hill.

Chatlynne, E., Rumigny, N., Amitay, M. & Glezer, A. 2001 Virtual aero-shapping of a clark-y airfoil using synthetic jet actuators. *Paper* 2001-0732. AIAA.

Chen, F. J. & Beeler, G. B. 2002 Virtual shaping of a two-dimensional naca 0015 airfoil using synthetic jet actuator. *Paper* 2002-3273. AIAA.

Collins, F. G. 1979 Boundary-layer control on wings using sound and leading edge serrations. *Paper* 79-1875. AIAA.

Darabi, A. & Wygnanski, I. 2002 On the transient process of flow reattachment by external excitation. *Paper* 2002-3163. AIAA.

Delery, J. M. 1985 Shock wave/turbulent boundary layer interaction and its control. *Prog. Aerosp. Sci.* **22**, 209–280.

Funk, R., Parekh, D., Crittenden, T. & Glezer, A. 2002 Transient separation control using pulse combustion actuation. *Paper* 2002-3166. AIAA.

Gad-El-Hak, M. 2000 *Flow Control: Passive, Active, and Reactive Flow Management*, 1st edn. Cambridge University Press.

Gad-El-Hak, M. & Bushnell, D. M. 1991 Separation control: review. *J. Fluids Engng* **113**, 5–30.

Gilarranz, J. L. & Rediniotis, O. K. 2001 Compact, high-power synthetic jet actuators for flow separation control. *Paper* 2001-0737. AIAA.

Glezer, A. & Amitay, M. 2002 Synthetic jets. *Annu. Rev. Fluid Mech.* **34**, 503–532.

Glezer, A., Amitay, M. & Honohan, A. M. 2003 Aspects of low- and high-frequency aerodynamic flow control. *Paper* 2003-0503. AIAA.

Greenblatt, D. & Wygnanski, I. 1999 Parameters affecting dynamic stall control by oscillatory excitation. *Paper* 99-3121. AIAA.

Greenblatt, D. & Wygnanski, I. 2003 Effect of leading-edge curvature on airfoil separation control. *J. Aircr.* **40**, 473–481.

Ham, F. & Iaccarino, G. 2004 Energy conservation in collocated discretization schemes on unstructured meshes. *Tech. Rep.* Annual Research Briefs 2004. Centre for Turbulence Research, Stanford University.

Ham, F., Mattson, K. & Iaccarino, G. 2006 Accurate and stable finite volume operators for unstructured flow solvers. *Tech. Rep.* Annual Research Briefs 2006. Centre for Turbulence Research, Stanford University.

He, Y. Y., Cary, A. W. & Peters, D. A. 2001 Parametric and dynamic modelling for synthetic jet control of a post-stall airfoil. *Paper* 2001-0733. AIAA.

Ho, C. M. & Huang, L. S. 1982 Subharmonics and vorted merging in mixing layers. *J. Fluid Mech.* **119**, 443–473.

Ho, C. M. & Huerre, P. 1984 Perturbed free shear layers. *Annu. Rev. Fluid Mech.* **16**, 365–424.

Johnson, W. S., Tennant, J. S. & Stamps, R. E 1975 Leading-edge rotating cylinder for boundary layer control on lifting surfaces. *J. Hydronaut.* **9**, 76–78.

Kaltenbach, H.-J., Fatica, M., Mittal, R., Lund, T. S. & Moin, P. 1999 Study of flow in a planar asymmetric diffuser using large-eddy simulation. *J. Fluid Mech.* **390**, 151–186.

Karypis, G., Schlogel, K. & Kumar, V. 2003 ParMETIS: parallel graph partitionaing and sparse matrix ordering library – Version 3.1. *Tech. Rep.* Department of Computer Science and Engineering, University of Minnesota, Minnesota, MN.

Katz, Y., Horev, E. & Wygnanski, I. 1992 The forced turbulent wall jet. *J. Fluid Mech.* **242**, 577–610.

Kotapati, R. B. 2008 On synthetic jets and their application to separation control in canonical airfoil flows. PhD thesis, The George Washington University, Washington, DC.

Kotapati, R. B., Mittal, R. & Ham, F. 2008 Large-eddy simulations of zero-net-mass-flux jet based separation control in a canonical separated flow. *Paper* 2008-4085. AIAA.

Kotapati, R. B., Mittal, R., Marxen, O., Ham, F. & You, D. 2007 Numerical simulations of synthetic jet based separation control in a canonical separated flow. *Paper* 2007-1308. AIAA.

Kourta, A., Boisson, H. C., Chassaing, P. & Minh, H. H. 1987 Nonlinear interaction and transition to turbulence in the wake of a circular cylinder. *J. Fluid Mech.* **181**, 141–161.

Maestrello, L., Badavi, F. F. & Noonan, K. W. 1988 Control of boundary layer separation about an airfoil by active surface heating. *Paper* 88-3545. AIAA.

Margalit, S., Greenblatt, D., Seifert, A. & Wygnanski, I. 2002 Active flow control of delta wing at high incidence using segmented piezoelectric actuators. *Paper* 2002-3270. AIAA.

McCullough, G. B. & Gault, D. E. 1951 Examples of three representative types of airfoil-section stall at low speed. *Tech. Rep.* TN 2502. NACA.

Miranda, S., Telionis, D. & Zeiger, M. 2001 Flow control of a sharp edged airfoil. *Paper* 2001-0119. AIAA.

Mittal, R., Venkatasubramanian, S. & Najjar, F. 2001 Large-eddy simulation of flow through a low-pressure turbine cascade. *Paper* 2001-2560. AIAA.

Na, Y. & Moin, P. 1998 Direct numerical simulation of a separated turbulent boundary layer. *J. Fluid Mech.* **370**, 175–201.

Najjar, F. M. & Vanka, S. P. 1993 Numerical study of separated-reattaching flow. *Theoret. Comput. Fluid Dyn.* **5**, 291–308.

Neuburger, D. & Wygnanski, I. 1987 The use of vibrating ribbon to delay separation on two-dimensional airfoils. In *Proceedings of Air Force Academy Workshop on Unsteady Separated Flow* (ed. J. M. Walker & F. J. Seiler). Colorado Springs, CO. *Tech. Rep.* 88-0004.

Nishri, B. 1995 On the dominant mechanisms governing active control of separation. PhD thesis, Department of Fluid Mechanics and Heat Transfer, Tel-Aviv University, Tel-Aviv, Israel.

Pack, L. G., Schaeffler, N., Yao, C. & Seifert, A. 2002 Active control of flow separation from the slat shoulder of a supercritical airfoil. *Paper* 2002-3156. AIAA.

Pack, L. G. & Seifert, A. 2000 Dynamics of active separation control at high Reynolds numbers. *Paper* 2000-0409. AIAA.

Postl, D., Gross, A. & Fasel, H. F. 2004 Numerical investigation of active flow control for low-pressure turbine blade separation. *Paper* 2004-0750. AIAA.

Prandtl, L. 1904 Über flüssigkeitsbewegung bei sehr kleiner reibung. In *Proceedings of Third International Congress of Mathematics*, Heidelberg, Germany, pp. 484–4918.

Prandtl, L. 1925 Magnuseffeckt und windkraftschiff. *Naturwissenschaften* **13**, 93–108.

Prandtl, L. 1935 The mechanics of viscous fluids. In *Aerodynamic Theory* (ed. W. F. Durand), pp. 34–208. Springer.

Prasad, A. & Williamson, C. H. K. 1996 The instability of the separated shear layer from a bluff body. *Phys. Fluids* **8**, 1347–1349.

Ravindran, S. S. 1999 Active control of flow separation over an airfoil. *Tech. Rep.* TM 209838. NACA.

Rizzetta, D. P. & Visbal, M. R. 2004 Numerical simulation of separation control for a transitional highly-loaded low-pressure turbine. *Paper* 2004-2204. AIAA.

Roshko, A. 1954 On the development of turbulent wakes from vortex sheets. *Tech. Rep.* No. 1191. NACA.

Schaeffler, N. W., Jenkins, L. N. & Hepner, T. E. 2004 Case 2: experimental evaluation of an isolated synthetic jet in crossflow. In *Proceedings of NASA LaRC Workshop on CFD Validation of Synthetic Jets and Turbulent Separation Control*, March 29–31, Williamsburg, VA.

Seifert, A., Bachar, T., Koss, D., Shepshelovich, M. & Wygnanski, I. 1993 Oscillatory blowing: a tool to delay boundary layer separation. *AIAA J.* **31**, 2052–2060.

Seifert, A., Darabi, A. & Wygnanski, I. 1996 Delay of airfoil stall by periodic excitation. *J. Aircr.* **33**, 691–699.

Seifert, A., Eliahu, S. & Greenblatt, D. 1998 Use of piezoelectric actuators for airfoil separation control. *AIAA J.* **36**, 1535–1537.

Seifert, A. & Pack, L. 1999 Oscillatory control of separation at high Reynolds numbers. *AIAA J.* **37**, 1062–1071.

Seifert, A. & Pack, L. 2000 Separation control at flight Reynolds numbers – lessons learned and future directions. *Paper* 2000-2542. AIAA.

Shepshelovich, M., Koss, D., Wygnanski, I. & Seifert, A. 1989 Active flow control on low re airfoils. *Paper* 89-0538. AIAA.

Sigurdson, L. W. & Roshko, A. 1985 Controlled unsteady excitation of a reattaching flow. *Paper* 85-0552. AIAA.

Sohn, K. H., Shyne, R. J. & DeWitt, K. J. 1998 Experimental investigation of boundary layer behaviour in a simulated low pressure turbine. *Paper* 98-GT-34. ASME.

Tian, Y., Cattafesta, L. & Mittal, R. 2006 Adaptive control of separated flow. *Paper* 2006-1401. AIAA.

Williamson, C. H. K., Wu, J. & Sheridan, J. 1995 Scaling of streamwise vortices in wakes. *Phys. Fluids* **7**, 2307–2309.

Wu, J. Z., Lu, X. Y., Denny, A. G., Fan, M. & Wu, J. M. 1998 Post-stall flow control on an airfoil by local unsteady forcing. *J. Fluid Mech.* **371**, 21–58.

Wu, J., Sheridan, J., Hourigan, K. & Soria, J. 1996 Shear layer vortices and longitudinal vortices in the near wake of a circular cylinder. *Exp. Therm. Fluid Sci.* **12**, 169–174.

Wygnanski, I. 1997 Boundary layer and flow control by periodic addition of momentum. *Paper* 97-2117. AIAA.

Wygnanski, I. 2000 Some new observations affecting the control of separation by periodic forcing. *Paper* 2000-2314. AIAA.

Zaman, K. B. M. Q., McKenzie, B. J. & Rumsey, C. L. 1989 A natural low frequency oscillation over airfoils near stalling conditions. *J. Fluid Mech.* **202**, 403–442.

Zhou, M. D. & Wygnanski, I. 1993 Parameters governing the turbulent wall jet in an external stream. *AIAA J.* **31**, 848–853.